



# **PennState**

## Applied Research Laboratory

### TECHNICAL REPORT/THESIS

#### A PRESCRIBED FLIGHT PERFORMANCE ASSESSMENT FOR UNDERSEA VEHICLE AUTOPILOT ROBUSTNESS

By

Daniel J. Bowman  
Dr. A. Scott Lewis

Approved for public release; distribution unlimited

The Pennsylvania State University  
The Applied Research Laboratory  
P. O. Box 30  
State College, PA 16804

A Prescribed Flight Performance Assessment for Undersea Vehicle Autopilot  
Robustness

By

Daniel J. Bowman  
Dr. A. Scott Lewis

Technical Report TR 16-002  
Date: 16 June 2016

Sponsored by: Applied Research Laboratory  
The Pennsylvania State University  
P.O. Box 30  
State College, PA 16804

Paul Sullivan, Director  
Applied Research Laboratory

Approved for public release; distribution unlimited

<b>REPORT DOCUMENTATION PAGE</b>				<i>Form Approved</i> OMB No. 0704-0188	
<p>The public reporting burden for this collection of information is estimated to average 1 hour per response, including the time for reviewing instructions, searching existing data sources, gathering and maintaining the data needed, and completing and reviewing the collection of information. Send comments regarding this burden estimate or any other aspect of this collection of information, including suggestions for reducing the burden, to the Department of Defense, Executive Service Directorate (0704-0188). Respondents should be aware that notwithstanding any other provision of law, no person shall be subject to any penalty for failing to comply with a collection of information if it does not display a currently valid OMB control number.</p> <p><b>PLEASE DO NOT RETURN YOUR FORM TO THE ABOVE ORGANIZATION.</b></p>					
<b>1. REPORT DATE</b> (DD-MM-YYYY)		<b>2. REPORT TYPE</b>		<b>3. DATES COVERED</b> (From - To)	
<b>4. TITLE AND SUBTITLE</b>				<b>5a. CONTRACT NUMBER</b>	
				<b>5b. GRANT NUMBER</b>	
				<b>5c. PROGRAM ELEMENT NUMBER</b>	
<b>6. AUTHOR(S)</b>				<b>5d. PROJECT NUMBER</b>	
				<b>5e. TASK NUMBER</b>	
				<b>5f. WORK UNIT NUMBER</b>	
<b>7. PERFORMING ORGANIZATION NAME(S) AND ADDRESS(ES)</b>				<b>8. PERFORMING ORGANIZATION REPORT NUMBER</b>	
<b>9. SPONSORING/MONITORING AGENCY NAME(S) AND ADDRESS(ES)</b>				<b>10. SPONSOR/MONITOR'S ACRONYM(S)</b>	
				<b>11. SPONSOR/MONITOR'S REPORT NUMBER(S)</b>	
<b>12. DISTRIBUTION/AVAILABILITY STATEMENT</b>					
<b>13. SUPPLEMENTARY NOTES</b>					
<b>14. ABSTRACT</b>					
<b>15. SUBJECT TERMS</b>					
<b>16. SECURITY CLASSIFICATION OF:</b>			<b>17. LIMITATION OF ABSTRACT</b>	<b>18. NUMBER OF PAGES</b>	<b>19a. NAME OF RESPONSIBLE PERSON</b>
<b>a. REPORT</b>	<b>b. ABSTRACT</b>	<b>c. THIS PAGE</b>			<b>19b. TELEPHONE NUMBER</b> (Include area code)

The Pennsylvania State University  
The Graduate School  
Mechanical and Nuclear Engineering Department

**A PRESCRIBED FLIGHT PERFORMANCE ASSESSMENT FOR UNDERSEA  
VEHICLE AUTOPILOT ROBUSTNESS**

A Thesis in  
Mechanical Engineering  
by  
Daniel J. Bowman

Submitted in Partial Fulfillment  
of the Requirements  
for the Degree of

Master of Science

August 2016

## ABSTRACT

Undersea vehicles are widely used in commercial and military applications to explore the open sea around the world. However, the modification of an existing design of an undersea vehicle for a specific application can be an intimidating task without a prescribed design assessment. Furthermore, operational use of a large class of the highly utilized axisymmetric undersea vehicle design sometimes requires unplanned and unforeseen mission payload weight and mass distribution changes. This research aims to provide the vehicle designer with a platform that enables faster implementation of confident design changes from an assessment while suppressing the level of uncertainty in resulting undersea vehicle flight performance and maneuverability. Unlike the narrow focus of many current undersea vehicle design assessments, this research simultaneously evaluates the broader impacts and benefits of changeability to common mechanical system design parameters and autopilot design. Two non-dimensional parameters that encompass the common changes to undersea vehicle weight configurations are defined. Additionally, the robustness of a well-tuned fixed weight configuration autopilot for an undersea vehicle is assessed against perturbed vehicle weight configuration models. Results are presented through evaluations of steady level flight, steady turn, and steady depth change flight performance simulations. The results suggest that a baseline autopilot is robust to changes in weight configuration but at the cost of steady state depth errors. The observed steady state depth errors are an outcome of the new trim characteristics of the perturbed weight configuration vehicle for which the baseline autopilot was not designed to accommodate. However, an offset compensation on the depth command to the autopilot enables the vehicle to attain desired depths. Ultimately, for a known typical range of unforeseen changes to an undersea vehicle's weight configuration a baseline autopilot can be very robust with the addition of offset compensations on the depth commands.

## TABLE OF CONTENTS

List of Figures .....	viii
List of Tables .....	x
Acknowledgements.....	xi
Chapter 1 INTRODUCTION.....	1
1.1 Background and Motivation .....	1
1.2 Review of Related Literature .....	4
1.3 Organization.....	6
Chapter 2 METHODS.....	7
2.1 Identification of a Generic Undersea Vehicle Model .....	7
2.2 Non-dimensional Vehicle Weight Configuration Parameters.....	9
2.3 Detailed Assessment Analysis .....	13
Chapter 3 LINEARIZATION OF A UV MODEL .....	16
3.1 Introduction.....	16
3.2 Vehicle Equations of Motion and Vehicle Body Forces and Moments.....	16
3.3 Linearized Equations of Motion .....	20
3.3.1 Yaw plane.....	21
3.3.2 Depth/Pitch Plane.....	23
3.3.3 Roll Axis .....	25
3.4 Linear Autopilot Architecture and Control Gains.....	26
3.4.1 Yaw plane Controller .....	27
3.4.2 Depth/Pitch Plane Controller .....	28
3.4.3 Roll Axis Controller.....	29
3.5 Summary.....	29
Chapter 4 HYDRODYNAMIC STABILITY DERIVATIVES.....	31
4.1 Introduction and Background .....	31
4.2 Detailed Summary .....	31
Chapter 5 NONLINEAR FLIGHT CONTROL MANEUVERING SIMULATION .....	35
5.1 Introduction.....	35
5.2 Inputs to the Simulation .....	35
5.3 Contents of the Simulation.....	36
5.4 Outputs of the Simulation .....	38
Chapter 6 ASSESSMENT TECHNIQUES & RESULTS.....	39
6.1 Introduction.....	39

6.2 Closed-loop Eigenvalue Analysis .....	39
6.2.1 Roll Axis .....	41
6.2.2 Depth/Pitch Plane.....	44
6.2.3 Yaw Plane .....	47
6.2.4 Summary of Eigenvalue Analysis .....	50
6.3 Flight Maneuvering Simulation Analysis .....	50
6.3.1 Steady Level Flight Simulation Results .....	52
6.3.2 Steady Turn Simulation Results .....	55
6.3.3 Steady Depth Change Simulation Results.....	57
6.4 Summary .....	61
Chapter 7 DISCUSSIONS & OBSERVATIONS.....	63
7.1 Governing Rules of Baseline Autopilot Robustness .....	63
7.2 Offset Depth Compensation and Results .....	63
7.3 Summary.....	70
Chapter 8 CONCLUSIONS & RECOMMENDATIONS .....	71
8.1 Conclusions.....	71
8.2 Recommendations.....	74
Appendix A.....	76
Glossary of Terms .....	76
Appendix B .....	80
Undersea Vehicle Hydrodynamic and Propulsor Model.....	80
Appendix C .....	83
Baseline Autopilot Controller Gains .....	83
Appendix D.....	84
Mission Command Sequences and Depth Compensation Gains.....	84
Bibliography .....	86

## LIST OF FIGURES

<b>Figure 1.1. UV Basic Mechanical Design Parameters .....</b>	<b>3</b>
<b>Figure 2.1. Isometric View of a 12.75 inch Generic UV Demonstration Model .....</b>	<b>8</b>
<b>Figure 2.2. Right-side View of a 12.75 inch Generic UV Demonstration Model.....</b>	<b>8</b>
<b>Figure 2.3. Propulsor View of a 12.75 inch Generic UV Demonstration Model .....</b>	<b>8</b>
<b>Figure 2.4. Typical Coordinate Convention for Undersea Vehicles.....</b>	<b>10</b>
<b>Figure 2.5. Graphical Depiction of the Vehicle Weight Configuration Space.....</b>	<b>12</b>
<b>Figure 2.6. Detailed Assessment Analysis for Undersea Vehicle Autopilot Robustness .....</b>	<b>13</b>
<b>Figure 3.1. Overall Procedure for Control Gain Determination .....</b>	<b>27</b>
<b>Figure 3.2. Yaw Plane Controller Block Diagram .....</b>	<b>28</b>
<b>Figure 3.3. Depth/Pitch Plane Controller Block Diagram.....</b>	<b>28</b>
<b>Figure 3.4. Roll Axis Controller Block Diagram.....</b>	<b>29</b>
<b>Figure 5.1. High Level Contents of Simulation .....</b>	<b>37</b>
<b>Figure 6.1. Roll Axis Closed-loop Eigenvalue Clustering, Low Speed .....</b>	<b>42</b>
<b>Figure 6.2. Roll Axis Closed-loop Eigenvalue Clustering, High Speed .....</b>	<b>43</b>
<b>Figure 6.3. Depth Plane Closed-loop Eigenvalue Clustering, Low Speed.....</b>	<b>45</b>
<b>Figure 6.4. Depth Plane Closed-loop Eigenvalue Clustering, High Speed.....</b>	<b>46</b>
<b>Figure 6.5. Yaw Plane Closed-loop Eigenvalue Clustering, Low Speed .....</b>	<b>48</b>
<b>Figure 6.6. Yaw Plane Closed-loop Eigenvalue Clustering, High Speed .....</b>	<b>49</b>
<b>Figure 6.7. Steady Level Flight: Speed and Depth Responses .....</b>	<b>53</b>
<b>Figure 6.8. Steady Level Flight: Elevator, Pitch Angle, and Pitch Rate Responses.....</b>	<b>54</b>
<b>Figure 6.9. Simple Diagram of Vertical Plane Forces in Steady Level Flight .....</b>	<b>55</b>
<b>Figure 6.10. Steady Turn: Rudder, Yaw Angle, and Yaw Rate Responses .....</b>	<b>56</b>
<b>Figure 6.11. Steady Turn: Speed and Depth Responses .....</b>	<b>57</b>
<b>Figure 6.12. Steady Depth Change: Speed and Depth Responses .....</b>	<b>58</b>



<b>Figure 6.13. Steady Depth Change: Elevator, Pitch Angle, and Pitch Rate Responses .....</b>	<b>59</b>
<b>Figure 6.14. Graphical Depiction of Observed Steady State Depth Errors for Each Vehicle Weight Configuration at Low Speed (10kt) .....</b>	<b>61</b>
<b>Figure 7.1. Offset Depth Command Compensation for Configuration 2B .....</b>	<b>64</b>
<b>Figure 7.2. Speed and Depth Responses with Depth Command Compensation .....</b>	<b>66</b>
<b>Figure 7.3. Elevator, Pitch, and Pitch Rate Responses with Depth Compensation .....</b>	<b>67</b>
<b>Figure 7.4. Five and Ten Meter Depth Change Evaluations with Depth Compensation .....</b>	<b>69</b>

## LIST OF TABLES

<b>Table 2-1. Generic Undersea Vehicle Basic Mechanical Properties and Dimensions .....</b>	<b>7</b>
<b>Table 2-2. Undersea Vehicle Weight Configuration Space .....</b>	<b>11</b>
<b>Table 6-1. Undersea Vehicle Standard Flight Performance Evaluations .....</b>	<b>51</b>
<b>Table 6-2. Mission Command Sequence for Steady Turn Evaluation .....</b>	<b>52</b>
<b>Table B-1. Generic Undersea Vehicle Hydrodynamic Simulation Model .....</b>	<b>80</b>
<b>Table B-2. Generic Undersea Vehicle Propulsor Simulation Model .....</b>	<b>82</b>
<b>Table C-1. Baseline Autopilot Controller Gains .....</b>	<b>83</b>
<b>Table D-1. Mission Command Sequences .....</b>	<b>84</b>
<b>Table D-2. Depth Compensation Gains .....</b>	<b>85</b>

## **ACKNOWLEDGEMENTS**

I would like to first gratefully acknowledge the support of the Pennsylvania State University Applied Research Laboratory (ARL). ARL provides excellent research opportunities for students and strongly encourages the pursuit of advanced degrees. I am truly grateful for the opportunities ARL has provided me to engage in research and development of elite engineering solutions.

I would like to thank Dr. A. Scott Lewis for all of his guidance, support, advice, and assistance throughout the course of this work. Additionally, I would like to thank Dr. Colin Begg for his gracious assistance throughout this work. I could not have completed this effort without the support of these two men and I greatly appreciate all of their help.

I would also like to thank Dr. Sean Brennan for serving as my faculty reader and for his time. His review and support of this work is greatly appreciated.

Lastly but most importantly, I would like to thank my family and friends for all of their love and support they have provided me throughout my education. I thank my parents for teaching me the importance of faith, hard work, and perseverance. Finally, I give honor to God and thank Him for the strength and comfort He has given me throughout my education.

## **Chapter 1**

### **INTRODUCTION**

#### **1.1 Background and Motivation**

Efficiency in any type of design modification is very important. Moreover, the development of governing rules of thumb for common design changes that affect the whole system is vital to reach a sufficient level of proficiency and confidence in those common changes. In many undersea vehicle (UV) applications unplanned or unforeseen changes to vehicle weight configuration do occur. These changes often include vehicle mission payload weight and vehicle mass distribution. For example, one could envision a UV being tasked with picking up or dropping off a payload. Another example related to this research effort involves the replacement of a UV mid-body by a heavier or lighter mid-body. Therefore, the UV's weight and mass distribution changes. It is important to note that changes to a UV's weight and mass distribution are much more frequent than changes to the vehicle geometry. For most axisymmetric UV designs in use today, the geometry of the vehicle hull and control surfaces are fixed designs. Thus, even though the weight or mass distribution of a UV may change, the vehicle hull and control surface geometries will not change. When these unplanned changes to a UV weight configuration are made, a full autopilot redesign validation cycle is often not possible. Therefore, mission critical flight maneuvering performance is often not fully considered. Ultimately, the unplanned changes in weight configuration to a UV can lead to an ineffective mission execution. Due to the prevalence of these unforeseen changes in UV mission payload weight and mass distribution, a fundamental approach will be outlined herein to evaluate the robustness of an original fixed vehicle weight configuration autopilot.

The following analogy can be used to set up the focus and desired outcome of this research. If a pilot of a small freight airplane decided to change the mass distribution or the weight of the freight payload to be different than the nominal distribution and weight, he would expect that he must compensate for these variations while flying the plane to maintain desired flight characteristics. Additionally, if the pilot increases the weight of the freight above the norm, the plane will not fly as typically expected. This same idea is being applied to UVs throughout this work. Furthermore, investigations into the robustness of an original fixed vehicle weight configuration autopilot design will be presented.

To that end, the unforeseen changes in weight configurations are typically applied to legacy vehicles whose autopilot has previously been well-tuned to meet desired flight performance metrics. The goal of this research is to evaluate how well an originally designed autopilot for a fixed UV weight configuration handles changes in vehicle payload weight and mass distribution. A baseline autopilot for an originally fixed weight configured vehicle is used throughout this work and evaluated across an acceptable configuration space of common changes in payload weight and mass distribution to UVs.

To assess UV flight performance to unplanned mission payload weight and mass distribution, the basic mechanical system parameters for UVs must be defined. Figure 1.1 depicts the basic mechanical system parameters surrounding changes to a UV's weight and mass distribution. The basic mechanical system parameters are defined within Figure 1.1 including weight,  $W$ , buoyancy,  $B_{uoy}$ , center of buoyancy, CB, center of mass, CM, and center of mass offset from the center of buoyancy,  $X_{CM}$ . An unforeseen change to a UV's weight and mass distribution is achieved by changing the payload weight,  $W_{payload}$ , or mass distribution via the center of mass offset from the center of buoyancy,  $X_{CM}$ . By convention, the center of buoyancy is the origin of the body fixed reference frame for UVs.

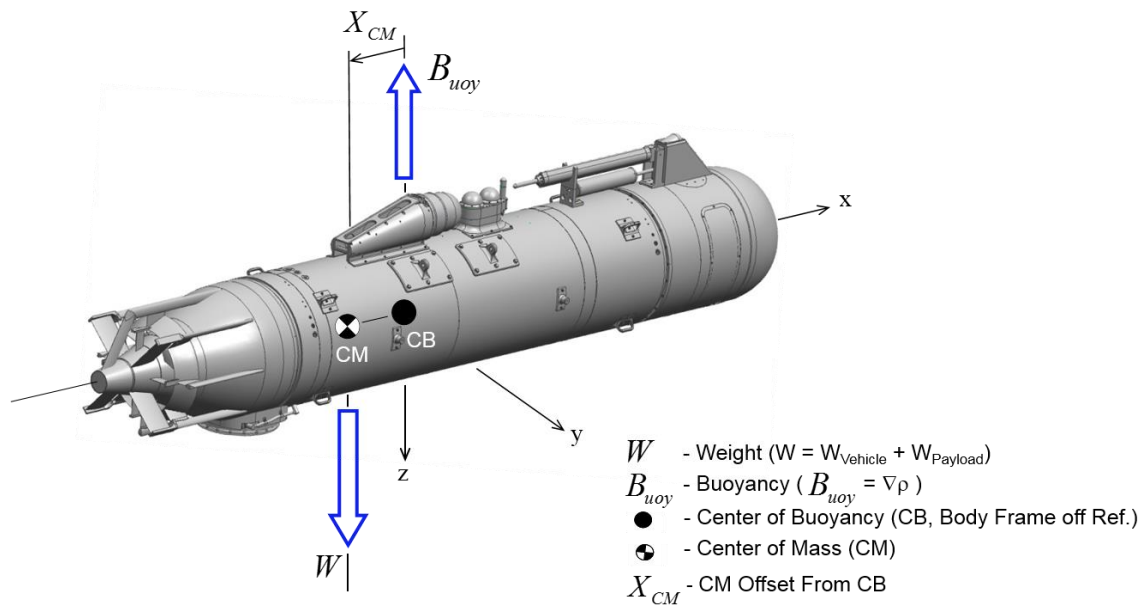


**Figure 1.1. UV Basic Mechanical Design Parameters**

Two non-dimensional parameters will be established in Chapter 2 that govern these changes to UV payload weight and mass distribution. A UV weight configuration space will also be introduced in Chapter 2 which encompasses the range of changes in vehicle payload weight and mass distribution for this study. A six degree of freedom (DOF) nonlinear flight maneuvering control simulation for a typically fixed hydrodynamic UV shell (hull) and control surface design will be used to assess payload and mass distribution changes that often arise during critical mission application executions. And finally, flight performance and maneuverability of a UV in all axes and planes of symmetry will be evaluated.

## 1.2 Review of Related Literature

Although UVs have been around for decades, much of the research found in recent literature does not address the fundamental problems that are often found in real mission critical applications such as changes in UV mission payload weight and mass distribution. Although the research herein presents a fundamental approach to address prevalent changes in UV mission payload weight and mass distribution, an aside is taken here to briefly discuss recent, relevant, and related research in UV flight control applications.

Current literature in the area of UV dynamics and control covers a large group of topics including path planning algorithms, nonlinear control techniques, integrated guidance navigation and control systems, and many more. Fernandes *et. al.* in [1] and [2] primarily focus on path planning, motion control, and high-gain observer design techniques for UV autopilots.

As with any dynamic system, there are governing equations of motion that contain model coefficients. For UVs, these coefficients, better known as hydrodynamic stability and control derivatives or hydro-coefficients, play a key role in the dynamic model of UVs. Hence, it is important to evaluate and study the sensitivity of these coefficients as in [3], which focuses on the sensitivity of these coefficients on surface ships, and [4] which studies the sensitivity of variations in hydro-coefficients on the maneuverability of submerged bodies. Chapter 4 will discuss hydrodynamic stability and control derivatives in more detail and reference how they are obtained. However, it is important to note upfront that hydrodynamic coefficients are governed by the geometric form of a UV. Hence, changes in UV mission payload weight and mass distribution do not affect the values of the dominant hydro-coefficients used in control design and evaluation.

Within [5] Petrich discusses the advantages and robustness of a second order model used in the pitch axis of a UV. Petrich also investigates different approaches to calibrate a tri-axial gyroscope and proposes a near real-time ocean current identification method to improve the

guidance of a UV. Petrich, as well as many others also discuss the implementation of  $H_\infty$  and sliding mode control algorithms, typically in a single plane of symmetry for UVs.

A control systems integration approach is presented by Fryxell *et. al.* in [6] on the integration of navigation, guidance, and control systems for autonomous undersea vehicles (AUVs). Discussions of multivariable control theory together with classical navigation and guidance techniques are presented and applied to a marine utility UV. The control of the presented marine utility vehicle consists of gain schedules around selected operating points and bounded by minimization of an  $H_\infty$  criterion.

Santhakumar in [7] investigates the influences on the dynamics and control caused by the addition of a robotic manipulator to an axisymmetric UV design. Dannigan in [8] produced a similar formulation of the dynamic coupling between a manipulator and a UV and presents the associated results of the manipulator-vehicle configuration.

The Monterey Bay Aquarium Research Institute (MBARI) performed some preliminary investigations of the influence of significant changes to the length of an axisymmetric UV. The model of interest consisted of exchangeable midsections which consequently influence the length of the UV. Although similar to the fundamental approach that will be presented herein, [9] primarily introduces the expected flight control issues that arise with a variable-length UV presenting only early-stage, preliminary results.

Prestero in [10] presents a very clear six DOF nonlinear simulation model of the REMUS autonomous underwater vehicle (AUV) utilizing a combination of experimental data and theory. Chapter 3 will discuss the linearization of a UV model including a very similar approach to that of Prestero. Others, such as Evans in [11] have taken a similar approach to produce dynamics models to simulate and evaluate the performance of a UV to avoid the expense of development and the risk involved in an experimental test.



The concentration of many of these recent research efforts in UV design focus on performance in a single axis or plane of symmetry of the vehicle. Thus, these design assessments presented in recent literature are performed with the awareness of dynamic coupling, but they cannot predict with great confidence the overall UV flight performance and maneuverability. The research presented herein differs from other research in that it approaches the UV design and autopilot robustness problem from a fundamental perspective focusing on the most common changes to axisymmetric UV weight configurations. Performance is evaluated holistically using a full six DOF nonlinear flight maneuvering simulation model to develop governing rules of thumb surrounding the robustness of an original fixed vehicle weight configuration autopilot to UV mission payload weight and mass distribution changes.

### **1.3 Organization**

The following chapter will outline the methods of the prescribed flight performance assessment for UV autopilot robustness. A discussion of the linearization of a highly nonlinear dynamic model of a UV will follow. Hydrodynamic stability and control derivatives are explained in Chapter 4 followed by an explanation of the six DOF nonlinear flight maneuvering simulation. Performance assessment techniques, results, and observations follow. Finally, summaries, conclusions, and recommendations for future work are presented.

## Chapter 2

### METHODS

#### 2.1 Identification of a Generic Undersea Vehicle Model

To assess through simulation the robustness of an original fixed UV weight configuration autopilot, a generic, neutrally buoyant, and evenly mass-distributed 12.75 inch diameter UV demonstration model was developed. Additionally, a well-tuned autopilot known to produce very good flight performance qualities was designed for this vehicle and was utilized as the baseline fixed UV weight configuration autopilot throughout the course of this research. More details on the autopilot structure and selection of controller gains will be presented in Chapter 3. Table 2-1 outlines the generic UV demonstration model including the basic mechanical properties and dimensions.

**Table 2-1. Generic Undersea Vehicle Basic Mechanical Properties and Dimensions**

Length:	3.66m (144in)
Weight:	285.3kg (629lbs)
Diameter:	0.3239m (12.75in) [axisymmetric circular cylinder major hull form]
Mass Moment of Inertia:	$I_{xx} = 1.5293\text{kg}\cdot\text{m}^2$ (1.1277slug-ft <sup>2</sup> ) $I_{yy} = I_{zz} = 232.98\text{kg}\cdot\text{m}^2$ (171.84slug-ft <sup>2</sup> )
Buoyancy:	285.3kg (629lbs)
Length from Nose to Center of Buoyancy:	1.76m (69.24in)
Center of Buoyancy to Tail Center of Lift:	1.6581m (65.28in)
Tail Configuration:	X Tail [four separately actuated full displacement control fins]
Propulsion:	Fixed, single, axially aligned, aft ducted thruster
Operational Speed Range	10 to 20kt (5.1 to 10.3m/s)

Collectively, the model does not represent any particular known vehicle in service today; however, some parameters are similar to those of a Remus 600 vehicle developed at the Woods Hole Oceanographic Institution. Geometric mesh rendering of isometric, right side, and propulsor views of the 12.75 inch diameter generic UV model can be seen in Figure 2.1, Figure 2.2, and Figure 2.3, respectively.

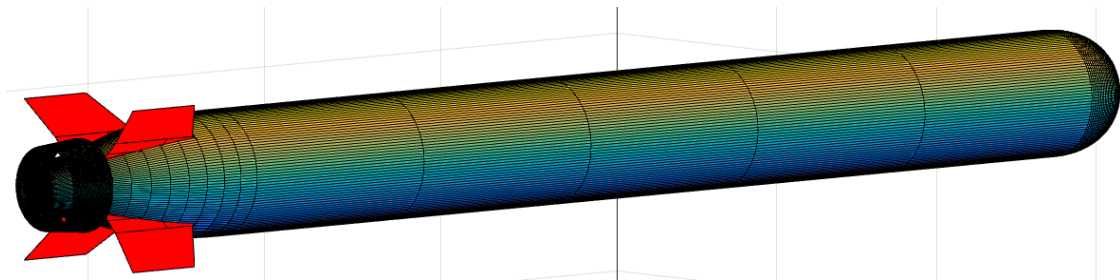


**Figure 2.1. Isometric View of a 12.75 inch Generic UV Demonstration Model**

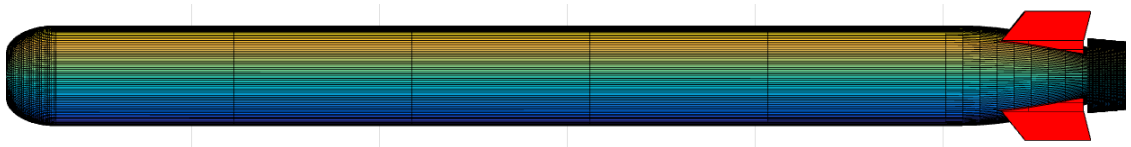


**Figure 2.2. Right-side View of a 12.75 inch Generic UV Demonstration Model**

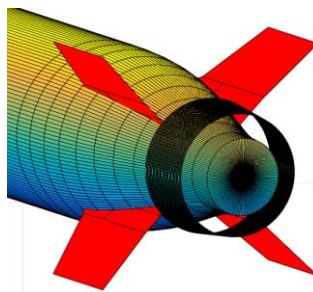


**Figure 2.3. Propulsor View of a 12.75 inch Generic UV Demonstration Model**

## 2.2 Non-dimensional Vehicle Weight Configuration Parameters

The scope of this research aims to evaluate the robustness of an original autopilot whose design was for a fixed vehicle weight configuration. To envelope the desired perturbation studies in UV weight configuration consisting of changes in vehicle payload weight and mass distribution, two non-dimensional parameters are defined. These two non-dimensional parameters are effective buoyancy,  $B_{eff}$ , and effective center of mass offset,  $X_{CM,eff}$ , shown in Equations 2.1 and 2.2.

$$B_{eff} = \left( 1 - \frac{W}{B_{uoy}} \right) \quad (2.1)$$

$$X_{CM,eff} = \left( \frac{-X_{CM}}{L} \right) \quad (2.2)$$

As defined, effective buoyancy is one minus the weight of the vehicle over the buoyancy of the vehicle. Hence, an effective buoyancy value of -0.1 is equivalent to the vehicle weight being 10 percent larger in magnitude than the buoyancy of the vehicle causing the vehicle to sink. Effective center of mass offset utilizes  $X_{CM}$ , the distance from the center of buoyancy (CB) to the center of mass (CM), and  $L$ , the overall length of the vehicle hull. It is important to note that  $x$  is defined to be positive in the forward direction of the vehicle. Hence, a negative valued  $X_{CM}$ , produces a positive valued  $X_{CM,eff}$ , therefore causing a positive pitching moment on the vehicle. To help clarify this notion, Figure 2.4 shows the typical right-handed, body-fixed coordinate system for UVs.

As expected, a change in vehicle payload weight will change the weight of the vehicle and a change in mass distribution will change the distance from the center of buoyancy to center of mass of the vehicle. High interest is placed on the robustness of an original baseline autopilot design

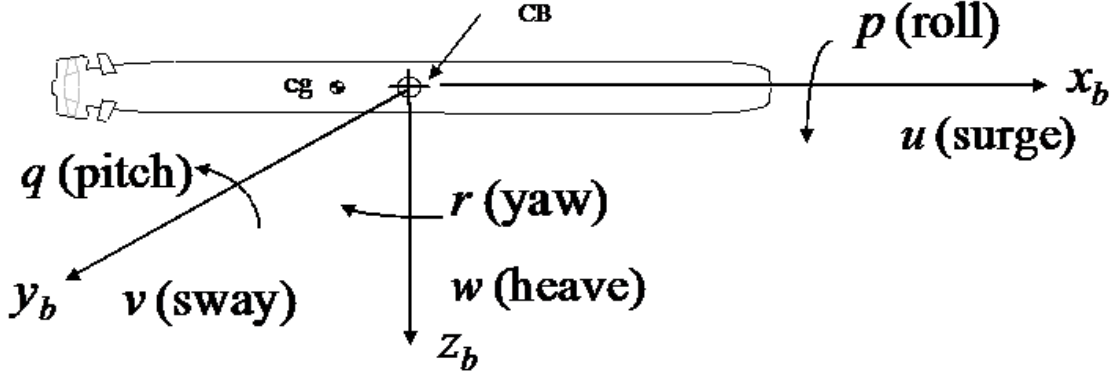


**Figure 2.4. Typical Coordinate Convention for Undersea Vehicles**

to the commonly unforeseen changes in  $W_{\text{payload}}$  and  $X_{\text{CM}}$  which are enveloped by the non-dimensional parameters  $B_{\text{eff}}$  and  $X_{\text{CM,eff}}$ . To test the robustness of a baseline autopilot, these two non-dimensional and basic mechanical system design parameters are varied within acceptable ranges of a typical weight configuration space for UVs. The typical unplanned adjustment ranges for  $B_{\text{eff}}$  and  $X_{\text{CM,eff}}$  are listed in Table 2-2. Moreover, Table 2-2 contains each corner of the weight configuration space used within the prescribed assessment of autopilot robustness. Also, Figure 2.5 contains a graphical depiction of the vehicle weight configuration space. Weight configuration 1A represents the fixed vehicle weight configuration for which the baseline autopilot was designed for the generic UV demonstration model. More specifically, the equivalent increases in  $W_{\text{payload}}$  and equivalent shifts forward and aft of the vehicle CM about the vehicle CB shown in Table 2-2 are in relation to the baseline weight configuration, 1A, of the generic UV demonstration model. The baseline autopilot is held constant to evaluate its robustness to the perturbed designs (i.e. models 1B through 2C). These five perturbed designs allow investigation of closed-loop flight performance impacts and an evaluation of the robustness of the baseline autopilot. Most UVs for operational application use are designed to be negatively buoyant. Additionally, for many UV applications there is a desire to increase the operational mission capability of the UV reflected by

an increase in the mission payload weight. Thus, for the purposes of this study, perturbations in effective buoyancy of the baseline model, 1A, create negatively buoyant perturbation models. In this way, the typical range of possible changes in an operational UV's buoyancy (neutral buoyancy to negative 10 percent buoyancy) are studied. However, both positive and negative displacements of the vehicle's center of mass are studied. Typically, operational UVs tend to be "tail heavy" meaning that the center of mass of the vehicle is shifted aft of the center of buoyancy due to the weight of the propulsion system aft of the center of buoyancy. Furthermore, the payload of a UV is usually located forward of the center of buoyancy. Hence, a change in the weight of the payload of a UV changes the location of the center of mass of the overall vehicle. And obviously, a heavier payload will shift the center of mass forward while a lighter payload will shift the center of mass in the aft direction. For the purposes of this study,  $X_{CM,eff}$  ranges from -0.04 to 0.01 covering the typical unforeseen range of changes to a UVs mass distribution while emphasizing increases in mission payload weight forward of the center of buoyancy.

**Table 2-2. Undersea Vehicle Weight Configuration Space**

Weight Configuration	$B_{eff}$	Equivalent Increase in $W_{payload}$ (lb)	$X_{CM,eff}$	Equivalent Shift of CM +fwd/-aft of CB (in)
1A*	0.00	0.00	0.00	0.00
1B	0.00	0.00	-0.04	+5.76
1C	0.00	0.00	+0.01	-1.44
2A	-0.10	62.90	0.00	0.00
2B	-0.10	62.90	-0.04	+5.76
2C	-0.10	62.90	+0.01	-1.44

\*1A represents the fixed weight configuration used to design the baseline autopilot for the 12.75 inch generic UV demonstration model

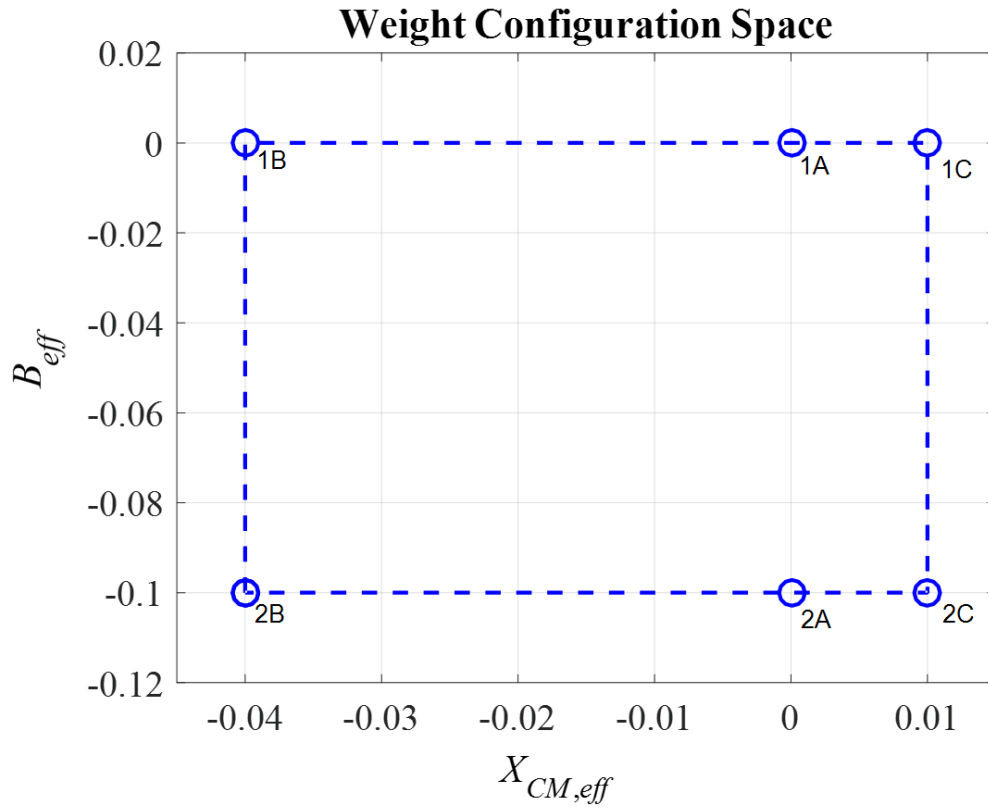


**Figure 2.5. Graphical Depiction of the Vehicle Weight Configuration Space**

Typically when unplanned changes in mechanical system parameters such as  $W_{payload}$  and  $X_{CM}$  occur, the hydrodynamic vehicle shell (hull) and fin geometry (control surfaces) are already fixed. Although design configurations involving varying shell and control fin geometries are not in the scope of the current analysis, it is important to note that the prescribed flight performance assessment can be used to study such UV geometry changes. These separate UV geometric changes comprised of varying shell and control fin geometries are significantly coupled to the hydrodynamic stability derivatives. For example, a change in geometric shape and surface area of the vehicle hull or control fins significantly impacts two sets of dominant hydrodynamic stability

coefficients in the depth/pitch and yaw planes of a UV. These hydrodynamic coefficients are discussed in more detail in Chapter 4.

### 2.3 Detailed Assessment Analysis

To assess the robustness of a fixed vehicle weight configuration autopilot a detailed flight performance assessment is utilized. This section will outline the rudiments of the assessment analysis. The assessment utilizes a full six DOF nonlinear undersea vehicle flight maneuvering simulation model coupled with a linear autopilot. This detailed assessment analysis can be seen in Figure 2.6. Moreover, the detailed assessment analysis is the foundation of the research presented herein. As with any dynamic system, the actual system dynamics are nonlinear and the same is

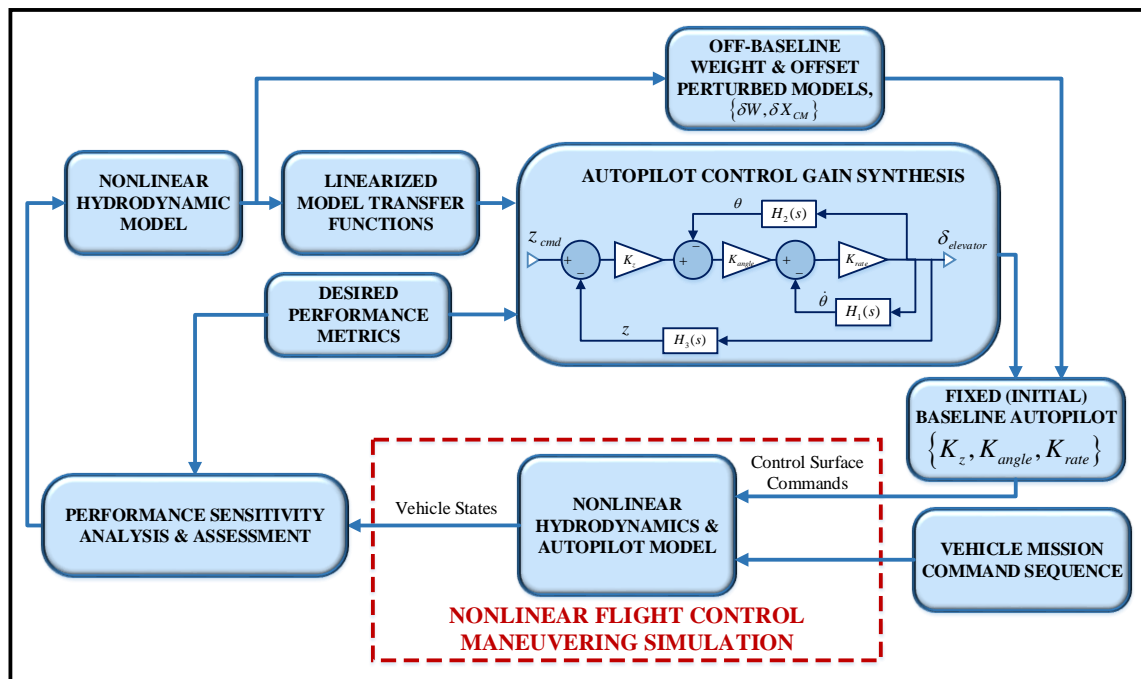


Figure 2.6. Detailed Assessment Analysis for Undersea Vehicle Autopilot Robustness



true of an undersea vehicle. Thus, the analysis begins with a highly nonlinear UV hydrodynamic model. For this study, the model is linearized to obtain linear model transfer functions following the approach that will be outlined in Chapter 3. Once a linear model is obtained and an autopilot architecture is selected, the appropriate control gains are computed to meet desired performance metrics such as specified overshoot, damping, and rise time. A discussion of the autopilot control architecture and selection of controller gains will be outlined in Chapter 3. At this point in the assessment, a baseline autopilot has been determined for a given UV model. The baseline fixed vehicle weight configuration autopilot for 12.75 inch diameter generic UV demonstration model was determined following this approach.

The next portion of the assessment analysis is the enabling driver for determining the robustness of the baseline autopilot to changes in UV weight configuration. This main driver is the six DOF nonlinear flight maneuvering simulation. Simulated vehicle responses to a mission command sequence are generated via the nonlinear flight maneuvering simulation. By examining the simulated performance of a vehicle, governing rules surrounding the robustness of a baseline autopilot can be determined. More details of the inputs, contents, outputs, and capability of the six DOF nonlinear flight maneuvering simulation will be discussed in Chapter 5.

Taking another look at the detailed assessment analysis, it is shown that the assessment is capable of perturbing an original nonlinear hydrodynamic UV model by changing the weight of the vehicle, the center of mass offset from the center of buoyancy, or both. These weight configuration changes are a result of desired changes to  $B_{eff}$  and  $X_{CM,eff}$  as outlined in section 2.2. After perturbing the nonlinear hydrodynamic model, the determination of a retuned autopilot controller gain set is not completed. The autopilot controller gain set remains unchanged. Hence, the baseline autopilot and control gain set designed for an originally fixed vehicle weight configuration (configuration 1A in this study) remains unchanged and is utilized by the newly configured vehicle

to evaluate flight performance impacts caused by changes in  $B_{eff}$  and  $X_{CM,eff}$ . The same mission command sequence is used and simulated flight performance is produced by the nonlinear flight control maneuvering simulation. Finally, the cycle is continued to evaluate the robustness of the original baseline autopilot to all of the perturbed vehicle weight configuration models. And because the baseline autopilot is utilized by each vehicle configuration, its robustness can be efficiently evaluated by comparing the simulated flight performance results of the baseline vehicle weight configuration to the results of each perturbed vehicle weight configuration.

## Chapter 3

### LINEARIZATION OF A UV MODEL

#### 3.1 Introduction

This section will show the derivation of linear dynamic models for the purpose of computing the autopilot speed-scheduled control gains. The fully-coupled, nonlinear equations of motion are presented and the assumptions and methods used to derive the linear set are explained. As previously shown in Figure 2.4, a standard right-handed, body-fixed coordinate system is used to derive the dynamic equations of motion for a generic underwater vehicle. The origin of the coordinate system is at the center of buoyancy (CB) of the vehicle and the center of gravity is denoted by cg.

#### 3.2 Vehicle Equations of Motion and Vehicle Body Forces and Moments

Within [10], Prestero describes the depth-plane linearization of the equations of motion and associated coefficients for a UV. Much of the linearization process presented here is an extension of that work by Prestero. The nonlinear equations of motion for a generic UV are based on the works of Feldman and Fossen within [12] and [13], respectively. It is important to note that some of the terms of the full six DOF nonlinear governing equations of motion presented within [12] are neglected here. The terms that are neglected are insignificant in magnitude for axisymmetric slender vehicles such as the 12.75 inch diameter generic UV demonstration model. The six nonlinear equations of motion can be written as

$$(m - X_{\ddot{u}})\dot{u} = F_x \quad (\text{surge}) \tag{3.1}$$

$$(m - Y_{\dot{v}})\dot{v} + (mx_g - Y_r)\dot{r} = F_y \quad (\text{sway}) \tag{3.2}$$

$$(m - Z_{\dot{w}})\dot{w} - (mx_g + Z_{\dot{q}})\dot{q} = F_z \quad (\text{heave}) \quad (3.3)$$

$$I_{xx}\dot{p} = M_x \quad (\text{roll}) \quad (3.4)$$

$$-(mx_g + M_{\dot{w}})\dot{w} + (I_{yy} - M_{\dot{q}})\dot{q} = M_y \quad (\text{pitch}) \quad (3.5)$$

$$(mx_g - N_{\dot{v}})\dot{v} + (I_{zz} - N_{\dot{r}})\dot{r} = M_z \quad (\text{yaw}) \quad (3.6)$$

where  $m$  is the vehicle mass and  $x_g$  is the distance from the center of buoyancy to the vehicle center of gravity along the  $x$  axis. A complete glossary of terms involved in the equations can be found in Appendix A. The added mass terms include  $X_{\dot{u}}, Y_{\dot{v}}, Y_{\dot{r}}, Z_{\dot{w}}, Z_{\dot{q}}, M_{\dot{w}}, M_{\dot{q}}, N_{\dot{v}}$  and  $N_{\dot{r}}$ .  $I_{xx}$ ,  $I_{yy}$ , and  $I_{zz}$  are the vehicle mass moments of inertia. In the derivation of the equations, it is assumed that the vehicle is predominantly axisymmetric. Moreover, the distance from the center of buoyancy to the center of gravity along the  $y$  axis,  $y_g$ , is zero. The distance from the center of buoyancy to the center of gravity along the  $z$  axis does have some small positive value to increase roll stability of the vehicle. However, the cross products of inertia,  $I_{xy}$ ,  $I_{xz}$ , and  $I_{yz}$  are negligible. The body forces and moments for Equations 3.1-3.6 are given by

$$\begin{aligned} F_x = & m(vr - wq - z_g pr + x_g (q^2 + r^2)) + X_{qq}q^2 + X_{rr}r^2 + X_{vr}vr + X_{wq}wq + X_{vv}v^2 + X_{ww}w^2 + \\ & X_{uu}u^2 + X_{uw\delta_e}uw\delta_e + X_{uq\delta_e}uq\delta_e + X_{uu\delta_e\delta_e}uu\delta_e^2 + X_{uv\delta_r}uv\delta_r + X_{ur\delta_r}ur\delta_r + X_{uu\delta_r\delta_r}uu\delta_r^2 + \\ & X_{uu\delta_s\delta_s}uu\delta_s^2 - (W - B_{uoy})\sin\theta + (1 - t_{ded})(T_{|n|n}n^2 + T_{|n|Va}n(1 - w)u) \quad (\text{surge}) \end{aligned} \quad (3.7)$$

$$\begin{aligned}
F_y = & m(wp - ur - z_g qr - x_g qp) + Y_{pq} pq + Y_{ur} ur + Y_{wp} wp + Y_{uv} uv + Y_{uu\delta_r} uu\delta_r + \\
& Y_{uv(\eta-1)} uv(\eta-1) + Y_{ur(\eta-1)} ur(\eta-1) + Y_{uu\delta_r(\eta-1)} uu\delta_r(\eta-1) + Y_{uvprop} uv_{prop} + \\
& \frac{\rho Y'_{cf}}{2} \int_0^L W_{C_D cf}(x) D(x) v(x) \sqrt{v^2(x) + w^2(x)} dx + (W - B_{uo_y}) \cos \theta \sin \phi \quad (\text{sway}) \quad (3.8)
\end{aligned}$$

$$\begin{aligned}
F_z = & m(uq - vp + z_g(p^2 + q^2) - x_g rp) + Z_{uq} uq + Z_{vp} vp + Z_{uw} uw + Z_{pr} pr + Z_{uu\delta_e} uu\delta_e + \\
& Z_{uw(\eta-1)} uw(\eta-1) + Z_{uq(\eta-1)} uq(\eta-1) + Z_{uu\delta_e(\eta-1)} uu\delta_e(\eta-1) + Z_{uwprop} uw_{prop} + \\
& \frac{\rho Z'_{cf}}{2} \int_0^L W_{C_D cf}(x) D(x) w(x) \sqrt{v^2(x) + w^2(x)} dx + (W - B_{uo_y}) \cos \theta \cos \phi \quad (\text{heave}) \quad (3.9)
\end{aligned}$$

$$\begin{aligned}
M_x = & (I_{yy} - I_{zz})qr + mz_g(ur - wp) + mx_g(vp - uq) + K_{up} up + K_{\sin(4\varphi_t)} V_t^2 \sin(4\varphi_t) + K_{uu\delta_s} uu\delta_s + \\
& K_{up(\eta-1)} up(\eta-1) + K_{uu\delta_s(\eta-1)} uu\delta_s(\eta-1) + K_{uu(\eta-1)} uu(\eta-1) + \\
& (1 - \eta_{stator})(Q_{|n|n} n^2 + Q_{|n|Va} n(1 - w)u) - z_g W \cos \theta \sin \phi \quad (\text{roll}) \quad (3.10)
\end{aligned}$$

$$\begin{aligned}
M_y = & (I_{zz} - I_{xx})rp + mz_g(vr - wq) + mx_g(vp - uq) + M_{rp} rp + M_{uq} uq + M_{uw} uw + M_{vp} vp + \\
& M_{uv\delta_s} uv\delta_s + M_{ur\delta_s} ur\delta_s + M_{uw(\eta-1)} uw(\eta-1) + M_{uq(\eta-1)} uq(\eta-1) + M_{uu\delta_e} uu\delta_e + \\
& M_{uu\delta_e(\eta-1)} uu\delta_e(\eta-1) + M_{uwprop} uw_{prop} - z_g W \sin \theta - W x_g \cos \theta \cos \varphi + \\
& \frac{\rho M'_{cf}}{2} \int_0^L W_{C_D cf}(x) D(x) w(x) \sqrt{v^2(x) + w^2(x)} x dx \quad (\text{pitch}) \quad (3.11)
\end{aligned}$$

$$\begin{aligned}
M_z = & (I_{xx} - I_{yy})pq + mx_g(wp - ur) + N_{pq}pq + N_{ur}ur + N_{uv}uv + N_{wp}wp + N_{uu\delta_r}uu\delta_r + \\
& N_{uw\delta_s}uw\delta_s + N_{uq\delta_s}uq\delta_s + N_{uv(\eta-1)}uv(\eta-1) + N_{ur(\eta-1)}ur(\eta-1) + \\
& N_{uu\delta_r(\eta-1)}uu\delta_r(\eta-1) + N_{uvprop}uv_{prop} + Wx_g \cos \theta \sin \varphi + \\
& \frac{\rho N'_{cf}}{2} \int_0^L W_{C_{Dcf}}(x) D(x) v(x) \sqrt{v^2(x) + w^2(x)} x dx \quad (\text{yaw}) \quad (3.12)
\end{aligned}$$

where  $\eta = u_c/u$  is the self-propulsion acceleration ratio between the commanded speed,  $u_c$ , and attained speed,  $u \approx V_t = \sqrt{u_t^2 + v_t^2 + w_t^2}$  denoting the velocity of the tail section. The integral terms, taken over the length,  $L$ , of the body involve crossflow terms where  $v(x) = v + xr$  and  $w(x) = w - xq$  and  $x$  represents the location along the length of the body. The diameter of the vehicle cross-section is denoted by  $D(x)$  and the respective crossflow drag coefficients are given by  $Y'_{cf}, Z'_{cf}, M'_{cf}$ , and  $N'_{cf}$ . The propeller velocities are given by  $v_{prop} = v + x_{prop}r$  and  $w_{prop} = w - x_{prop}q$ . The subscripted terms denoted by  $X, Y, Z, K, M$ , and  $N$  represent the hydrodynamic coefficients. The restoring forces, weight and buoyancy of the vehicle, are denoted by  $W$  and  $B_{uoy}$ , respectively. The last terms in Equation 3.7 are concerned with the propulsion of the vehicle and  $\sin(4\phi_t) = 4v_t w_t (w_t^2 + v_t^2) / V_t^4$  where  $t$  denotes the tail section. The fin deflections for splay, rudder, and elevator are denoted by  $\delta_s, \delta_r$ , and  $\delta_e$ , respectively.

These equations with the Euler equations presented in [13] describe the physical model. The Euler equations result from a three rotation sequence (zyx-convention) whereby the vehicle is rotated about the z-axis by an angle  $\psi$ , then rotated about the y-axis by an angle  $\theta$ , and then finally about the x-axis by an angle  $\phi$  where it is noted that the order of these rotations does matter. In essence, these rotations result in the vehicle being rotated from the North-East-Down (NED)

coordinate system to the body fixed frame. Equations 3.13 and 3.14 show the relationship between the two coordinate systems as a function of the Euler angles.

$$\begin{bmatrix} \dot{x} \\ \dot{y} \\ \dot{z} \end{bmatrix} = \begin{bmatrix} \cos\psi \cos\theta & -\sin\psi \cos\phi + \cos\psi \sin\theta \sin\phi & \sin\psi \sin\phi + \cos\psi \cos\phi \sin\theta \\ \sin\psi \cos\theta & \cos\psi \cos\phi + \sin\phi \sin\psi \sin\theta & -\cos\psi \sin\phi + \sin\theta \sin\psi \cos\phi \\ -\sin\theta & \cos\theta \sin\phi & \cos\theta \cos\phi \end{bmatrix} \begin{bmatrix} u \\ v \\ w \end{bmatrix} \quad (3.13)$$

$$\begin{bmatrix} \dot{\phi} \\ \dot{\theta} \\ \dot{\psi} \end{bmatrix} = \begin{bmatrix} 1 & \sin\phi \tan\theta & \cos\phi \tan\theta \\ 0 & \cos\phi & -\sin\phi \\ 0 & \sin\phi / \cos\theta & \cos\phi / \cos\theta \end{bmatrix} \begin{bmatrix} p \\ q \\ r \end{bmatrix} \quad (3.14)$$

### 3.3 Linearized Equations of Motion

In order to simplify control gain selection, linear models are derived for the yaw and depth/pitch planes and the roll axis. Although the crossflow terms have been described in the previous section, they are small enough in magnitude to be appropriately neglected in the linearized model and in the determination of autopilot controller gains. In general, the steady forward speed  $U$  of the vehicle will be large compared to the other components of velocity. For linearization purposes, the linear and angular velocities can be written as

$$u(t) = U + \hat{u} \quad (3.15)$$

$$v(t) = \hat{v} \quad (3.16)$$

$$w(t) = \hat{w} \quad (3.17)$$

$$p(t) = \hat{p} \quad (3.18)$$

$$q(t) = \hat{q} \quad (3.19)$$

$$r(t) = \hat{r} \quad (3.20)$$

where the hat variables represent small perturbations from the operating point. The yaw and depth planes as well as the roll axis equations will now be derived. In each case, any terms out of plane are ignored.

### 3.3.1 Yaw plane

The yaw plane equations contain the variables  $u$ ,  $v$ , and  $r$  and any terms involving  $w$ ,  $p$ , and  $q$  are ignored. As a result, Equations 3.1, 3.2, and 3.6 go to the following, respectively.

$$(m - X_{\dot{u}})\dot{u} = m(vr + x_g r^2) + X_{rr}r^2 + X_{vr}vr + X_{vv}v^2 + X_{uu}u^2 + X_{uv\delta r}uv\delta_r + X_{ur\delta r}ur\delta_r + X_{uu\delta r\delta r}uu\delta_r^2 \quad (\text{surge}) \quad (3.21)$$

$$(m - Y_{\dot{v}})\dot{v} + (mx_g - Y_{\dot{r}})\dot{r} = -mur + Y_{ur}ur + Y_{uv}uv + Y_{uu\delta r}uu\delta_r + Y_{uv(\eta-1)}uv(\eta-1) + Y_{ur(\eta-1)}ur(\eta-1) + Y_{uu\delta r(\eta-1)}uu\delta_r(\eta-1) + Y_{uvprop}uv_{prop} \quad (\text{sway}) \quad (3.22)$$

$$(mx_g - N_{\dot{v}})\dot{v} + (I_{zz} - N_{\dot{r}})\dot{r} = -mx_g ur + N_{ur}ur + N_{uv}uv + N_{uu\delta r}uu\delta_r + N_{uv(\eta-1)}uv(\eta-1) + N_{ur(\eta-1)}ur(\eta-1) + N_{uu\delta r(\eta-1)}uu\delta_r(\eta-1) + N_{uvprop}uv_{prop} \quad (\text{yaw}) \quad (3.23)$$

By ignoring higher order terms, and any constant terms, Equations 3.21, 3.22, and 3.23 can be simplified further as

$$(m - X_{\dot{u}})\dot{u} = 2X_{uu}Uu \quad (\text{surge}) \quad (3.24)$$

$$(m - Y_{\dot{v}})\dot{v} + (mx_g - Y_{\dot{r}})\dot{r} = -mUr + Y_{ur}Ur + Y_{uv}Uv + Y_{uu\delta r}U^2\delta_r + Y_{uvprop}U(v + x_{prop}r) \quad (\text{sway}) \quad (3.25)$$



$$(mx_g - N_{\dot{v}})\dot{v} + (I_{zz} - N_{\dot{r}})\dot{r} = -mx_g Ur + N_{ur}Ur + N_{uv}Uv +$$

$$N_{uu\delta r}U^2\delta_r + N_{uvprop}U(v + x_{prop}r) \quad (\text{yaw}) \quad (3.26)$$

From Equations 3.13 and 3.14 for small angles, the following linear Euler, yaw plane equations are obtained

$$\dot{y} = U\psi + v \quad (3.27)$$

$$\dot{\psi} = r \quad (3.28)$$

The surge equation, Equation 3.24, is not needed in the equations of motion since it is decoupled from sway and yaw. As a result Equations 3.25-3.28 can be put into matrix form as

$$\begin{bmatrix} m - Y_{\dot{v}} & mx_g - Y_{\dot{r}} & 0 & 0 \\ mx_g - N_{\dot{v}} & I_{zz} - N_{\dot{r}} & 0 & 0 \\ 0 & 0 & 1 & 0 \\ 0 & 0 & 0 & 1 \end{bmatrix} \begin{bmatrix} \dot{v} \\ \dot{r} \\ \dot{y} \\ \dot{\psi} \end{bmatrix} =$$

$$\begin{bmatrix} (Y_{uv} + Y_{uvprop})U & (Y_{ur} - m + Y_{uvprop}x_{prop})U & 0 & 0 \\ (N_{uv} + N_{uvprop})U & (-mx_g + N_{ur} + N_{uvprop}x_{prop})U & 0 & 0 \\ 1 & 0 & 0 & U \\ 0 & 1 & 0 & 0 \end{bmatrix} \begin{bmatrix} v \\ r \\ y \\ \psi \end{bmatrix} = \begin{bmatrix} Y_{uu\delta r}U^2 \\ N_{uu\delta r}U^2 \\ 0 \\ 0 \end{bmatrix} \delta_r \quad (3.29)$$

In compact form, Equation 3.29 can be written as

$$M\dot{x} = C_d x + \bar{B}\delta_r \quad (3.30)$$

Equation 3.30 can be expressed in the traditional state space form as

$$\dot{x} = M^{-1}C_d x + M^{-1}\bar{B}\delta_r = Ax + B\delta_r \quad (3.31)$$

where the notations are obvious.

### 3.3.2 Depth/Pitch Plane

For the depth plane, the variables  $u$ ,  $w$ , and  $q$  are retained and any terms involving  $v$ ,  $p$  or  $r$  are ignored. As a result, Equations 3.1, 3.3, and 3.5 reduce to

$$(m - X_{\dot{u}})\dot{u} = 2X_{uu}Uu - (W - B_{uoy})\theta \quad (\text{surge}) \quad (3.32)$$

$$(m - Z_{\dot{w}})\dot{w} - (mx_g + Z_{\dot{q}})\dot{q} = mUq + Z_{uq}Uq + Z_{uw}Uw + \\ Z_{uu\delta_e}U^2\delta_e + Z_{uwprop}U(w - x_{prop}q) + (W - B_{uoy})\theta \quad (\text{heave}) \quad (3.33)$$

$$-(mx_g + M_{\dot{w}})\dot{w} + (I_{yy} - M_{\dot{q}})\dot{q} = -mx_gUq + M_{uq}Uq + M_{uw}Uw - z_gW\theta + \\ M_{uwprop}U(w - x_{prop}q) \quad (\text{pitch}) \quad (3.34)$$

From Equations 3.13 and 3.14, the following linear Euler, pitch plane equations are obtained

$$\dot{z} = -U\theta + w \quad (3.35)$$

$$\dot{\theta} = q \quad (3.36)$$

It is noted that heave and pitch are decoupled from surge. As a result Equations 3.33-3.36 can be put into matrix form as

$$\begin{bmatrix} m - Z_{\dot{w}} & -mx_g - Z_{\dot{q}} & 0 & 0 \\ -mx_g - M_{\dot{w}} & I_{yy} - M_{\dot{q}} & 0 & 0 \\ 0 & 0 & 1 & 0 \\ 0 & 0 & 0 & 1 \end{bmatrix} \begin{bmatrix} \dot{w} \\ \dot{q} \\ \dot{z} \\ \dot{\theta} \end{bmatrix} = \begin{bmatrix} (Z_{uw} + Z_{uwprop})U & (Z_{uq} + m - Z_{uwprop}x_{prop})U & 0 & W - B_{uoy} \\ (M_{uw} + M_{uwprop})U & (M_{uq} - mx_g - M_{uwprop}x_{prop})U & 0 & -z_g W \\ 1 & 0 & 0 & -U \\ 0 & 1 & 0 & 0 \end{bmatrix} \begin{bmatrix} w \\ q \\ z \\ \theta \end{bmatrix} \\
 = \begin{bmatrix} Z_{uu\delta e} U^2 \\ M_{uu\delta e} U^2 \\ 0 \\ 0 \end{bmatrix} \delta_e \quad (3.37)$$

In compact form, Equation 3.37 can be written as

$$M\dot{x} = C_d x + \bar{B}\delta_e \quad (3.38)$$

Equation 3.38 can be expressed in traditional state space form as

$$\dot{x} = M^{-1}C_d x + M^{-1}\bar{B}\delta_e = Ax + B\delta_e \quad (3.39)$$

where the notations are obvious.

### 3.3.3 Roll Axis

Equations 3.2, 3.3 and 3.4 describing the roll axis contain the variables  $u, v, w$ , and  $p$  and any term involving  $q$  and  $r$  is ignored.

$$(m - Y_{\dot{v}})\dot{v} - Y_{\dot{p}}\dot{p} = Y_{uv}Uv + Y_{uvprop}Uv + (W - B_{uoy})\phi \quad (\text{sway}) \quad (3.40)$$

$$(m - Z_{\dot{w}})\dot{w} = Z_{uw}Uw + Z_{uwprop}Uw \quad (\text{heave}) \quad (3.41)$$

$$I_{xx}\dot{p} = K_{up}Up + K_{uu\delta s}U^2\delta_s - z_g W\phi \quad (\text{roll}) \quad (3.42)$$

From Equations 3.13 and 3.14 for small angles, the linear Euler equations for the roll axis are obtained

$$\dot{z} = w \quad (3.43)$$

$$\dot{\phi} = p \quad (3.44)$$

Equation 3.41 is decoupled from the other variables, thus only Equations 3.40, 3.42 and 3.44 are needed to represent the roll axis. In matrix form, they can be expressed as

$$\begin{bmatrix} m - Y_{\dot{v}} & -mz_g - y_{\dot{p}} & 0 \\ -mz_g - k_{\dot{v}} & I_{xx} - k_{\dot{p}} & 0 \\ 0 & 0 & 1 \end{bmatrix} \begin{bmatrix} \dot{v} \\ \dot{p} \\ \dot{\phi} \end{bmatrix} - \begin{bmatrix} (Y_{uvprop} + Y_{uv})U & 0 & W - B_{uoy} \\ 0 & K_{up}U & -z_g W \\ 0 & 1 & 0 \end{bmatrix} \begin{bmatrix} v \\ p \\ \phi \end{bmatrix} = \begin{bmatrix} 0 \\ K_{uu\delta s}U^2 \\ 0 \end{bmatrix} \delta_s \quad (3.45)$$

More compactly, Equation (45) can be expressed as

$$M\dot{x} - C_d x = \bar{B}\delta_s \quad (3.46)$$

Equation 3.46 can be written in the traditional state space form as

$$\dot{x} = M^{-1}C_d x + M^{-1}\bar{B}\delta_s = Ax + B\delta_s \quad (3.47)$$

where the notations are obvious.

### 3.4 Linear Autopilot Architecture and Control Gains

The pertinent open loop transfer functions necessary for controlling the yaw and depth/pitch planes and the roll axis can be obtained by taking the LaPlace Transform on both sides of equations 3.31, 3.39, and 3.47, respectively. Additionally, the main goal of this research is to assess the robustness of a well-tuned, fixed UV weight configuration autopilot constructed from those transfer functions with appropriate feedback loops. A summary of the overall procedure for determining the autopilot controller gains is shown in Figure 3.1. The structure of the autopilot and determination of well-tuned controller gains is not the main focus of this research effort. For completeness however, a high level outline of the autopilot architecture for the generic UV demonstration model introduced in Chapter 2 will be presented in this section accompanied by a brief explanation of the determination of controller gains. Furthermore, it is important to note that the fixed vehicle weight configuration autopilot was designed for the original generic demonstration model (weight configuration 1A) presented in section 2.1. The generic UV demonstration model is neutrally buoyant and evenly mass distributed meaning that the weight of the vehicle is equivalent to the buoyancy of the vehicle and the center of mass location of the vehicle is very close to the center of buoyancy location of the vehicle. A small offset from the center of buoyancy to the center of mass along the  $z$  axis does exist, but is negligible in the control gain computation for the generic UV demonstration model. Hence, some of the terms within the

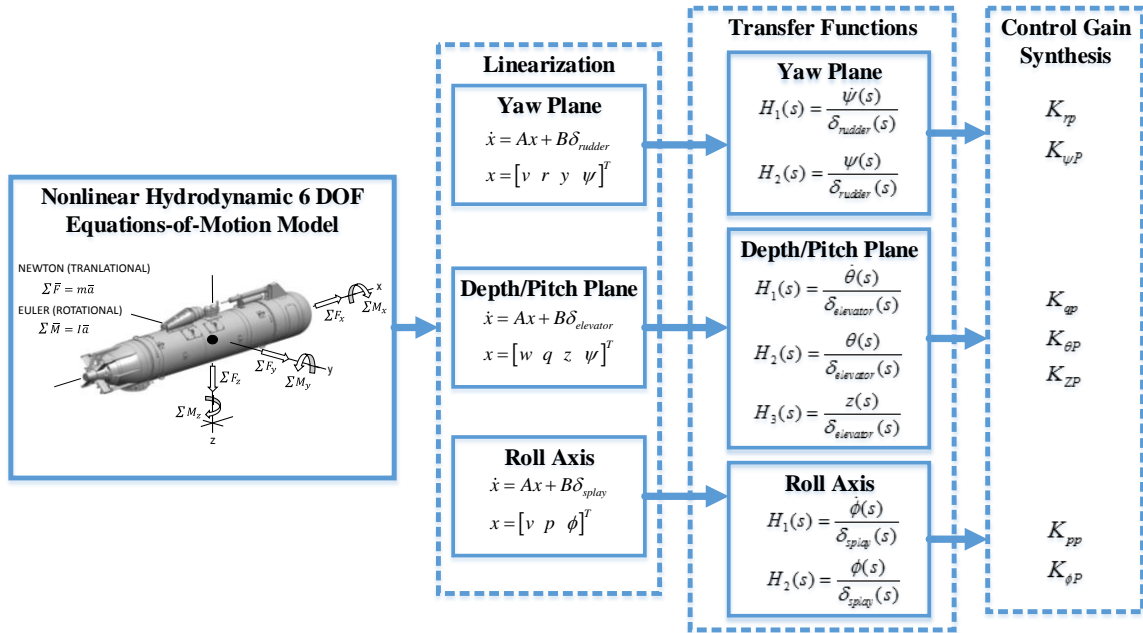


**Figure 3.1. Overall Procedure for Control Gain Determination**

equations presented in section 3.3 are negligible in the design of the baseline fixed weight configuration autopilot for the generic UV simulation model.

### 3.4.1 Yaw plane Controller

The yaw plane utilizes two successive feedback loops as shown in Figure 3.2. The inner loop controls the yaw rate while the outer loop controls the yaw attitude. The gains for each loop are computed such that the closed-loop eigenvalues of the yaw plane are stable and exhibit maximized damping. The gains are also selected such that the rise time of a response in yaw angle is minimized. Damping is maximized to minimize overshoot of the vehicle response when trying to attain a commanded yaw angle. Steady state error is also minimized by the selection of the controller gains.

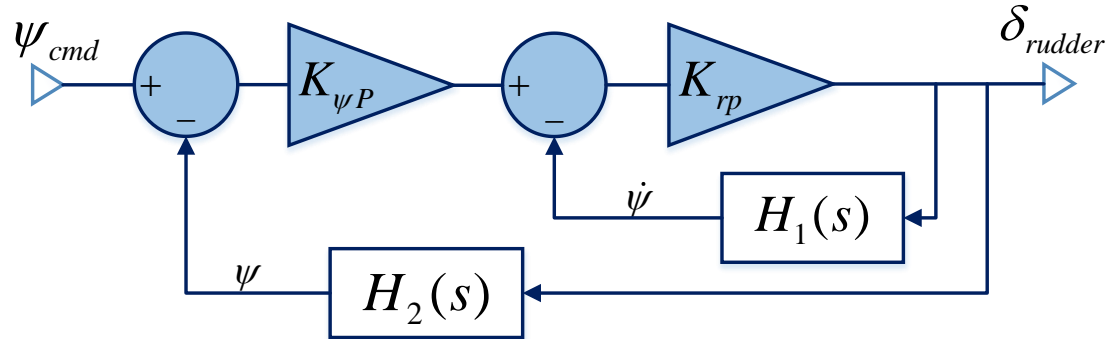


**Figure 3.2. Yaw Plane Controller Block Diagram**

### 3.4.2 Depth/Pitch Plane Controller

Similar to the yaw plane controller, the depth/pitch plane controller utilizes three successive feedback loops as shown in Figure 3.3. The inner-most loop controls the pitch rate, the second loop closure controls the pitch attitude, and the third loop closure controls depth, or the  $z$  position of the vehicle. The gains for each loop are computed such that the closed-loop eigenvalues of the depth/pitch plane are stable and exhibit maximized damping. The gains are also selected such that the rise time of a response in depth and steady state depth error are minimized. Damping is maximized to minimize overshoot of the vehicle response when trying to attain a commanded depth.

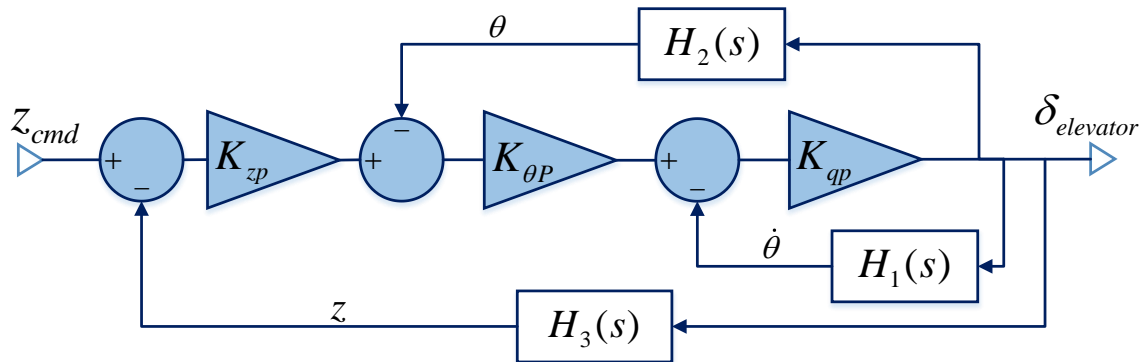


**Figure 3.3. Depth/Pitch Plane Controller Block Diagram**

### 3.4.3 Roll Axis Controller

Again, similar to the yaw plane controller, the roll axis controller utilizes two successive feedback loops as shown in Figure 3.4. The inner loop controls the roll rate and the outer loop controls the roll attitude. The gains for each loop are computed such that the closed-loop eigenvalues of the system are stable and exhibit maximized damping. In many UV applications it is highly desirable to maintain stability of the roll axis at a near zero roll attitude at all times.

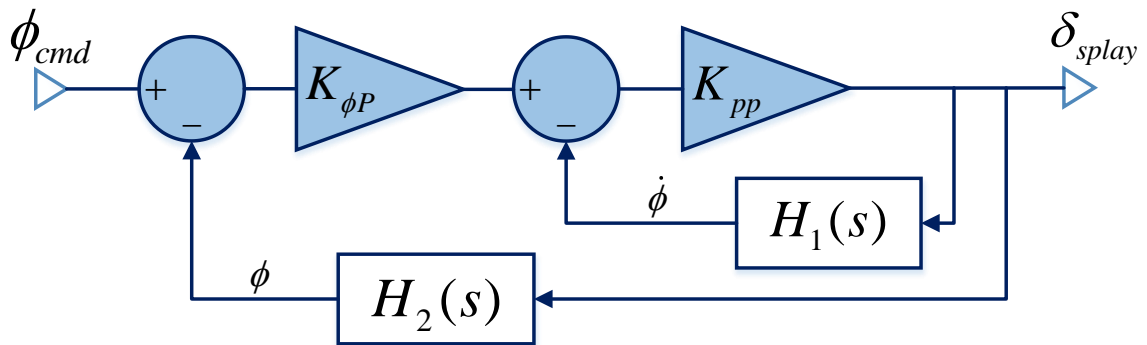


Figure 3.4. Roll Axis Controller Block Diagram

## 3.5 Summary

This chapter has derived linear models describing the dynamics of an undersea vehicle to support control gain calculation. Nonlinear crossflow terms have been omitted as they are typically negligible within the computation of autopilot control gains. However, future work could investigate if the inclusion of the crossflow terms into a control scheme can improve vehicle performance. A high level outline of the autopilot architecture for each plane/axis of the 12.75 inch diameter demonstration model introduced in Chapter 2 was presented accompanied by a brief explanation of the determination of controller gains in each axis. A complete set of controller gains for the baseline autopilot of the generic UV demonstration model can be found in Appendix C.



Finally, the closed-loop transfer functions for the roll axis, depth/pitch plane, and yaw plane can be seen in Chapter 6.

## Chapter 4

### HYDRODYNAMIC STABILITY DERIVATIVES

#### 4.1 Introduction and Background

The governing equations of motion of any dynamic system contain modeling coefficients. Furthermore, the governing equations of motion for a UV were shown in detail in Chapter 3. Also, the nonlinear flight maneuvering simulation used throughout this research contains the full six DOF model of the governing equations of motion to accurately simulate the motion of a UV. Within those equations presented in Chapter 3, the subscripted terms denoted by  $X$ ,  $Y$ ,  $Z$ ,  $K$ ,  $M$ , and  $N$  represent the hydrodynamic stability derivatives, also known as hydrodynamic coefficients. This chapter will briefly discuss what hydrodynamic coefficients are and reference how they are determined.

#### 4.2 Detailed Summary

An extensive use of mathematical models are used to describe the governing differential equations for stability and control of submerged bodies. These differential equations are comprised of numerous coefficients or derivatives which are of hydrodynamic origin. As a result, accurate solutions to these governing equations require knowledge of the coefficients or hydrodynamic stability derivatives to a reasonable level of accuracy [14]. The hydrodynamic forces and moments which enter into the governing differential equations of motion of a submerged body are characterized by stability and control derivatives. Hydrodynamic stability and control derivatives take the form of partial derivatives of a force or moment with respect to a vehicle motion parameter or control surface input parameter. Static, rotary, and acceleration are the three usual categories

that the hydrodynamic forces and moments can be placed into. Static in this sense refers to those coefficients that are a result of linear velocity of a submerged body relative to the surrounding fluid. Angular velocity of a submerged body relative to a surrounding fluid produces the rotary coefficients and likewise, acceleration relative to the surrounding fluid of a submerged body produces acceleration or added mass coefficients. Within limited ranges, the coefficients are linear with respect to the associated motion variable and thus may be utilized as their respective derivatives within the linearized differential equations that govern the motion of a submerged body in a fluid. In short, these coefficients represent models within certain ranges of associated variables to describe the relative forces and moments produced on a submerged body in motion by the surrounding fluid. The coefficients are essentially models that comprise the body linearized force and moment components acting on a vehicle relative to a quasi-steady operating condition. As an example,  $M_{uw}$  represents a derivative of a moment component in the pitch axis of a submerged body with respect to the velocity components  $u$  and  $w$  of the body relative to the surrounding fluid. In other words,  $M_{uw}$  is a model contained in a single coefficient that describes the pitching moment that a submerged body would experience if it was performing a quasi-steady, straight-line forward flight maneuver and a perturbation was applied to  $w$ . Ultimately,  $M_{uw}$  in its mathematical notation can be written as  $\frac{\partial^2 M}{\partial u \partial w}$ .

By revisiting Equations 3.3 and 3.9, the entire heave, or Z-force equation of motion for submerged vehicles can be shown as seen in Equation 4.1. One can now examine all of the major hydrodynamic coefficients involved in just one governing equation of the nonlinear six DOF model and the associated categories of the hydrodynamic coefficients.

$$\begin{aligned}
(m - Z_{\dot{w}})\dot{w} - (mx_g + Z_{\dot{q}})\dot{q} = & \quad \text{(Added Mass Coefficient Terms)} \\
m(uq - vp + z_g(p^2 + q^2) - x_g rp) + & \quad \text{(Inertial, Coriolis, and Centripetal Terms)} \\
Z_{uq}uq + Z_{vp}vp + Z_{uw}uw + Z_{pr}pr + Z_{uu\delta_e}uu\delta_e + \\
Z_{uw(\eta-1)}uw(\eta-1) + Z_{uq(\eta-1)}uq(\eta-1) + Z_{uu\delta_e(\eta-1)}uu\delta_e(\eta-1) + Z_{uwprop}uw_{prop} + \\
\frac{\rho Z'_{cf}}{2} \int_0^L W_{C_{Dcf}}(x) D(x) w(x) \sqrt{v^2(x) + w^2(x)} dx + & \quad \text{(Static and Rotary Coefficient Terms)} \\
(W - B_{uoy}) \cos \theta \cos \varphi & \quad \text{(Restoring Terms)} \quad (4.1)
\end{aligned}$$

Hydrodynamic coefficients are typically best determined using experimental techniques. These experimental techniques involve a physical model of a vehicle being submerged and towed through a fluid at various angles of attack and performing standard maneuvers to measure the forces and moments exerted on the vehicle by the surrounding fluid. A more detailed explanation including examples of the determination of hydrodynamic coefficients can be found in [14]. Results within [14] also show the linearity of hydrodynamic coefficients with respect to the associated motion variable over an acceptable range. This linearity of hydrodynamic coefficients is important as it improves the validity of linearized differential equations that govern the motion of a submerged body in a fluid.

During the twentieth century there was a growing effort to develop a straightforward design method for submerged vehicle dynamic stability, performance, and ease of handling. Within [14], Goodman explains that there was a lack of straightforward techniques to obtain desirable submerged body characteristics to meet desired performance metrics. Goodman's paper explains many of the advancements that were made during the twentieth century for the determination of hydrodynamic coefficients including the Planar-Motion-Mechanism System at The David Taylor Model Basin. The David Taylor Model Basin in Carderock, MD continues to be the leading

research center investigating various experimental techniques and simulation based methods of analysis to predict hydrodynamic stability and control derivatives of submerged bodies. To that end, there have been numerous advances of computer-aided estimation of hydrodynamic coefficients. Moreover, the hydrodynamics coefficients of the generic UV demonstration model used for this research were determined using best engineering semi-empirical estimation methods. Also, the model form follows that which is used in standard undersea vehicle system modeling similar to those found in [12] and [15]. A full list of the hydrodynamic coefficients of the demonstration model can be found in Appendix B.

## **Chapter 5**

### **NONLINEAR FLIGHT CONTROL MANEUVERING SIMULATION**

#### **5.1 Introduction**

As discussed in previous chapters, a complete nonlinear flight control maneuvering simulation is the empowering driver of this research. The simulation, developed using the MathWorks product, Simulink, enables efficient evaluation of the robustness of a baseline autopilot to perturbed UV weight configurations. A set of inputs can be supplied to the simulation. The simulation can then employ those inputs to simulate a predetermined flight performance mission. Finally, the outputs generated by the simulation are utilized for the assessment analysis. This chapter will discuss the inputs, contents, and outputs of the nonlinear flight control maneuvering simulation.

#### **5.2 Inputs to the Simulation**

The nonlinear flight control maneuvering simulation requires several inputs. The first of these inputs is a complete set of the hydrodynamic coefficients and basic mechanical properties of a nonlinear UV model. Hydrodynamic coefficients, as described in Chapter 4, are the modeling coefficients within the governing equations of motion of a UV. The simulation includes the full nonlinear six DOF equations of motion of a UV to accurately simulate a vehicle's response to commanded inputs. Therefore, a UV's hydrodynamic coefficients and basic mechanical properties must be supplied to the simulation as inputs. A second set of inputs to the simulation includes actuator and propulsor dynamic modeling coefficients which also enter into the governing equations of motion to determine accurate simulation results. The third set of inputs to the flight

maneuvering simulation are the initial conditions and desired mission command sequence for a prescribed flight performance evaluation. Initial conditions supplied to the simulation include the initialized dynamic states of the vehicle for the prescribed flight performance evaluation including body positions, velocities, and accelerations, body attitudes, body angle rates and accelerations, control surface deflection angles, and the initial propulsor RPM. The mission command sequence supplied to the simulation includes the commanded roll angle, pitch angle, yaw angle, pitch rate, yaw rate, propulsor RPM, and depth for specified durations. A more detailed explanation including an example of a mission command sequence for a desired flight performance maneuver is presented in Chapter 6. Finally, a set of autopilot controller gains for each plane/axis of a UV over a predetermined range of speeds must be supplied to the simulation model. If each input is appropriately supplied to the nonlinear flight maneuvering simulation, then the contents of the simulation are able to accurately develop a simulated response of a UV to the directed maneuvers within the mission command sequence.

### **5.3 Contents of the Simulation**

The contents of the nonlinear flight control maneuvering simulation enable efficient evaluation of a UV's flight performance to a desired mission command sequence. Within the simulation is a series of nested modules interlinked to take a set of inputs, process those inputs, and solve for the resulting dynamic state of vehicle. At the highest level, the simulation consists of a nonlinear UV dynamics model module and a controller module as seen in Figure 5.1. The nonlinear UV dynamics module includes all of the nested dynamics of a UV dynamic model including the actuator and propulsor dynamics. A fundamental sub-module of the dynamics module is the equations of motion solver tasked with solving the nonlinear six DOF governing equations of motion of a UV. Outputs of the UV dynamics module, comprised of the dynamic states of the

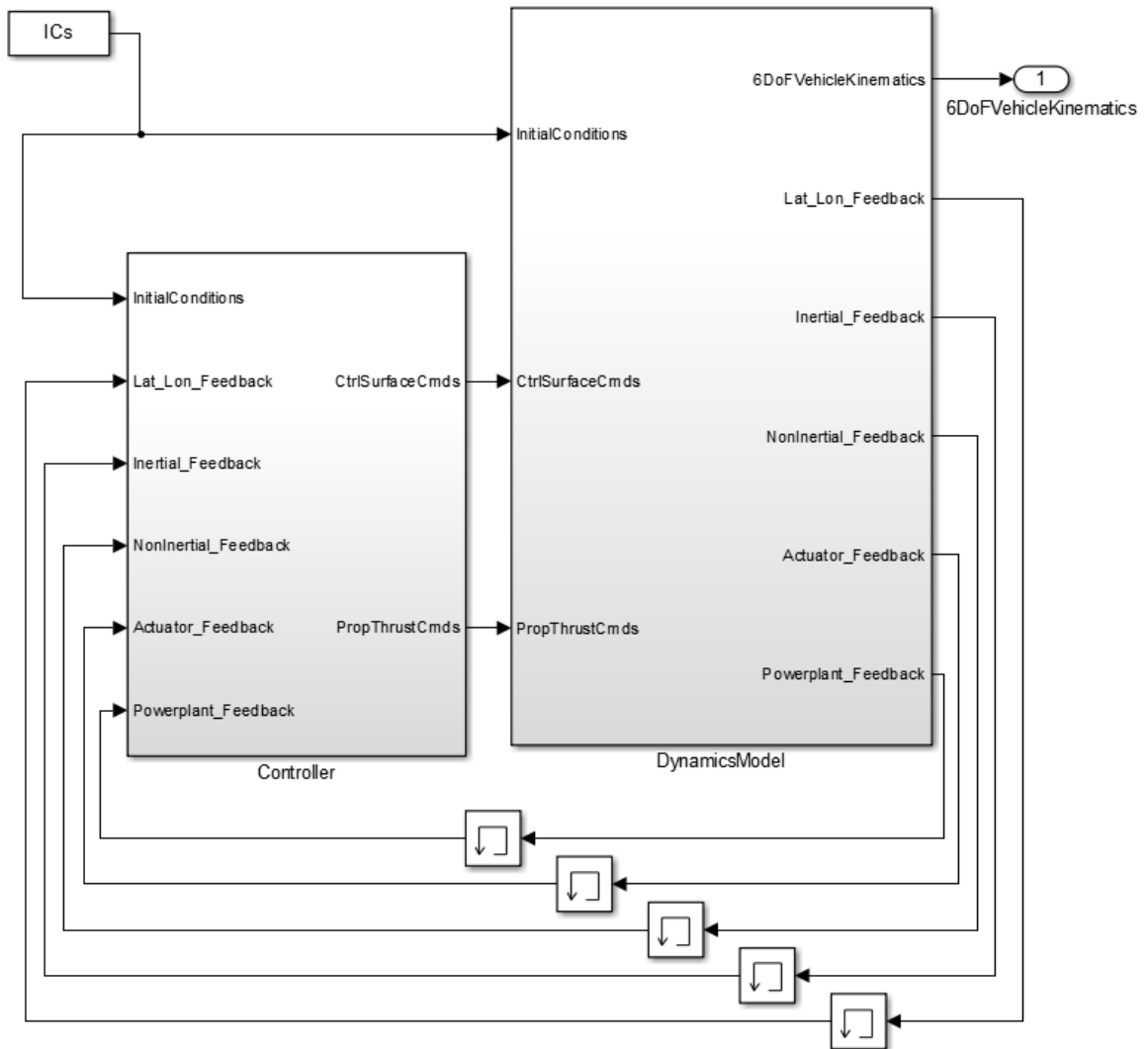


**Figure 5.1. High Level Contents of Simulation**

UV, are fed back to the controller module where compensation of errors in commanded versus actual dynamic states is performed by the autopilot.

The controller module contains the controller for each plane/axis as outlined in section 3.4. Each plane/axis controller accepts the commanded input from the mission command sequence, compares it to the actual dynamic state of the UV, and performs its designed compensation to produce commanded changes in control surface deflections. Commanded changes in the UV's



control surface deflections are then sent to the UV dynamics module. Within the UV dynamics module, the actual control surface deflections are dictated by the actuator dynamics. For the purposes of this study, near ideal actuator dynamics are utilized. Finally, the actual control surface deflections are utilized by the equations of motion solver to determine the resulting changes in the vehicle dynamic states. Ultimately, changes in control surface deflections drive the vehicle to the commanded dynamic state of the mission command sequence.

#### **5.4 Outputs of the Simulation**

Simulated vehicle responses to a mission command sequence are generated by the nonlinear flight maneuvering simulation. Outputs of the simulation include the simulated results of body positions, velocities, and accelerations, body attitudes, body angle rates and accelerations, control surface deflection angles, propulsor RPM, and speed. The resulting outputs of the simulation reflect the simulated dynamic states of the vehicle as it completes the prescribed maneuvers contained in the mission command sequence.

## Chapter 6

### ASSESSMENT TECHNIQUES & RESULTS

#### 6.1 Introduction

This research focuses on the development of a fundamental approach to assess the robustness of an undersea vehicle autopilot to unforeseen mission payload weight and mass distribution changes. The framework for this autopilot robustness assessment approach has been outlined in the previous chapters. With the established framework for the assessment in place, the detailed assessment techniques and results of the autopilot robustness assessment will now be addressed.

#### 6.2 Closed-loop Eigenvalue Analysis

Dynamic systems are always uncertain in some capacity. Moreover, variations of components of a dynamic system can lead to parametric uncertainty within the system model. For the purposes of this study, the defined non-dimensional parameters effective buoyancy,  $B_{eff}$ , and effective center of mass offset,  $X_{CM,eff}$ , represent the vulnerability of existing UV designs to unforeseen changes in weight configuration. In essence, the unexpected changes to a UV's weight configuration can be thought of as a parametric uncertainties in the weight or center of mass location of a UV.

Extensive research conducted in the 1980s and 1990s investigated the robustness of dynamic systems to uncertainties. The field of robust control significantly grew during this time including methods such as  $\mu$  synthesis,  $H_\infty$  control, Kharitonov polynomial methods, and

quadratic stability [16]. Moreover, when multiple uncertain parameters exist in a system, the complexity of determining bounds for robust stability measures increases significantly. In fact, within [16] Yedavalli dedicates an entire section in the second chapter of his book on the various approaches to determine the appropriate bounds for robust stability analysis. However, robust performance and resulting stability of a system can be evaluated more fundamentally by examining the root clustering, or closed-loop eigenvalue locations of a system in the complex plane as the uncertain parameters are varied. Since the typical range of variations in effective buoyancy and effective center of mass offset are predetermined for the course of this study, an analysis of closed-loop eigenvalue cluster locations is performed.

The locations of the closed-loop eigenvalue clusters in each plane and axis of the 12.75 inch generic UV demonstration model were determined by computing the closed-loop eigenvalues of each perturbed weight configuration model outlined in Table 2-2. To analyze autopilot robustness, the controller gains of the well-tuned, baseline autopilot designed for the unperturbed UV demonstration model were held constant for the computation of the closed-loop eigenvalues and zeros of each perturbed weight configuration model. Furthermore, closed-loop eigenvalues of the depth/pitch and yaw planes and roll axis of the UV models were determined at the lowest operational speed (10kt) and highest operational speed (20kt). Although not shown here, the mid-speed eigenvalue locations exhibit very similar modal damping and natural frequency characteristics with a few exceptions that will be discussed in the following sections. For completeness and to gain a better understanding of overall closed-loop dynamics, the closed-loop zeros and poles (eigenvalues) are plotted to show the impacts of changes in  $B_{eff}$  and  $X_{CM,eff}$ .

### 6.2.1 Roll Axis

Figure 6.1 and Figure 6.2 show the closed-loop clusters of the poles and zeros of the overall linear transfer function in the roll axis at low speed and high speed, respectively. Furthermore, Equations 6.1 to 6.4 describe the closed-loop transfer function for the roll axis where notations are obvious. As seen in the plots, the perturbations in weight configuration had very little influence on

$$\frac{\delta_{splay}(s)}{\phi_{cmd}(s)} = \frac{K_{\phi P} K_{pp} (s^3 - (A_{11} + A_{22})s^2 + A_{11}A_{22})}{s^3 + h_1 s^2 + h_2 s + h_3} \quad (6.1)$$

where

$$h_1 = K_{pp} b_2 - (A_{11} + A_{22}) \quad (6.2)$$

$$h_2 = A_{11}A_{22} - A_{21}A_{12} - A_{23}A_{32} + K_{pp} (A_{21}b_1 - A_{11}b_2) + K_{\phi P} K_{pp} b_2 \quad (6.3)$$

$$h_3 = K_{\phi P} K_{pp} (A_{21}b_1 - A_{11}b_2) + A_{11}A_{23}A_{32} - A_{21}A_{13}A_{32} \quad (6.4)$$

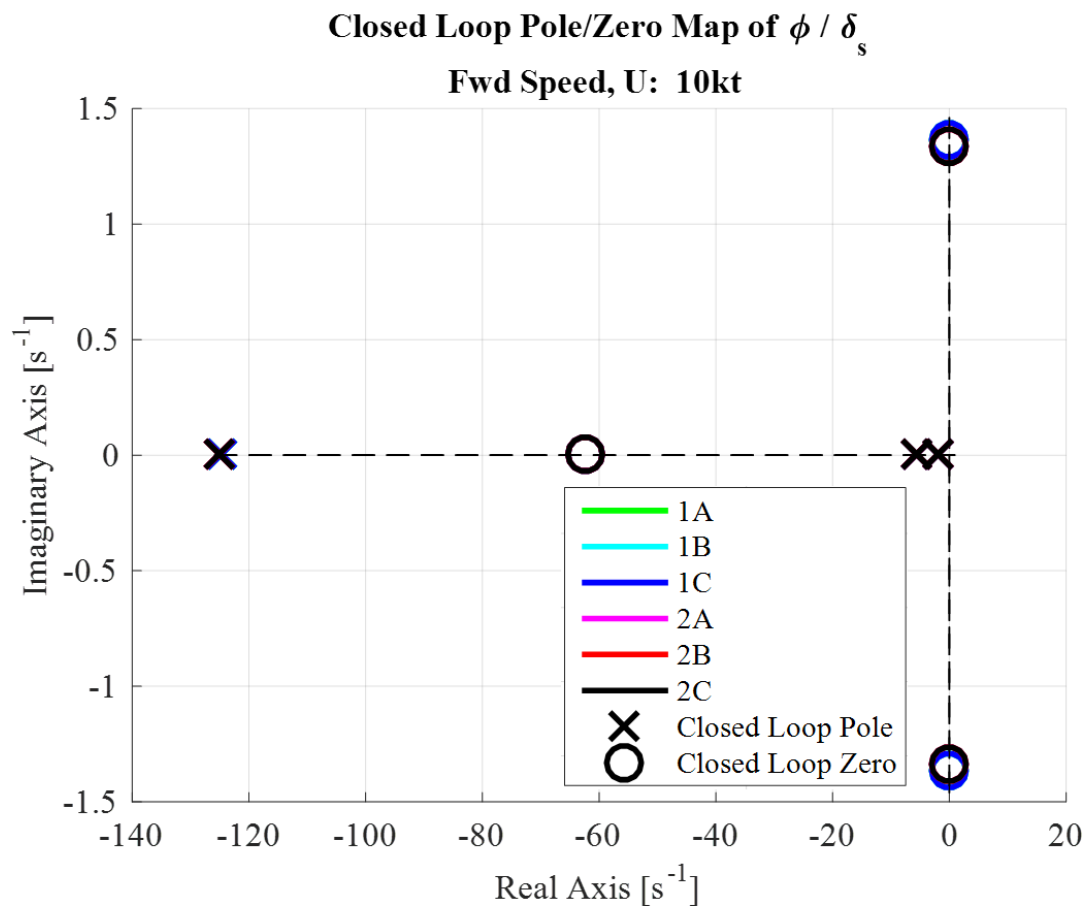


**Figure 6.1. Roll Axis Closed-loop Eigenvalue Clustering, Low Speed**

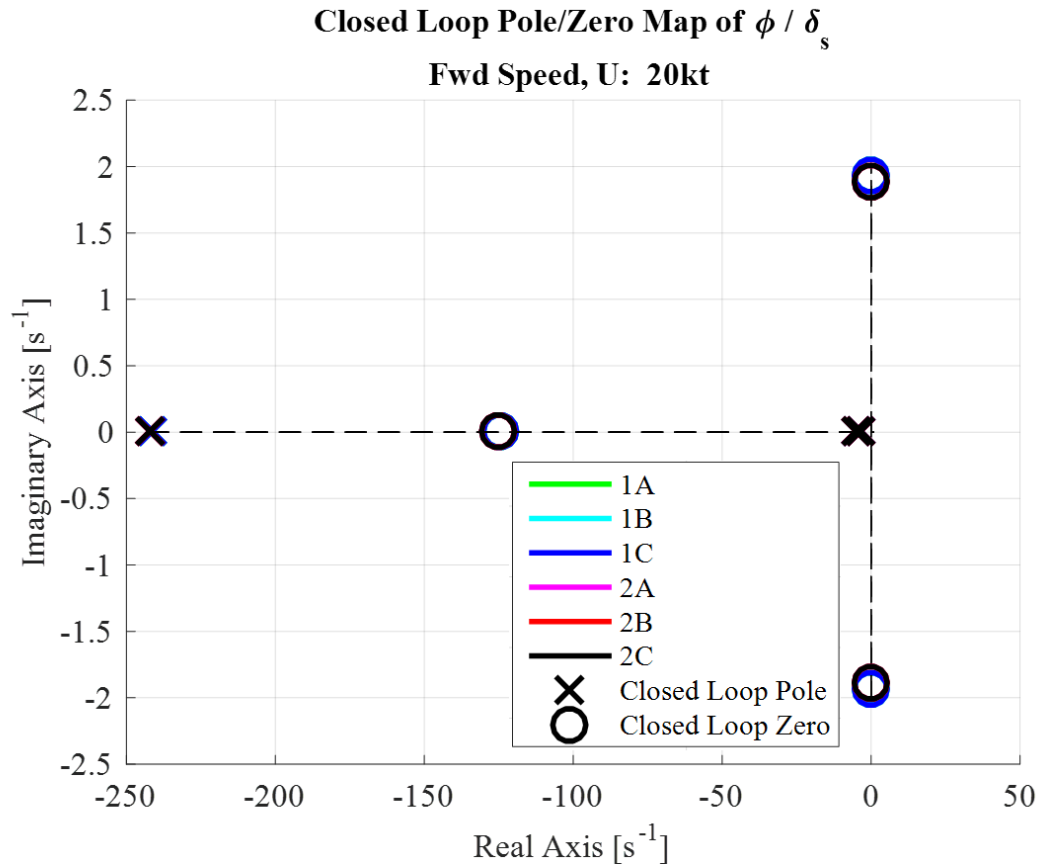


**Figure 6.2. Roll Axis Closed-loop Eigenvalue Clustering, High Speed**

the locations of closed-loop poles. The closed-loop poles exhibit maximized damping characteristics based on the selection of the controller gains for the baseline UV demonstration model. Moreover, the poles are critically damped at low speed and remain critically damped at high speed while changing in natural frequency. These results in the roll axis suggest that the fixed weight configuration autopilot maintains stability and virtually no change in roll axis performance when the specified weight configuration changes are made to the vehicle.

### 6.2.2 Depth/Pitch Plane

When weight configuration changes are made to the vehicle we see small impacts on the closed-loop eigenvalues in the depth/pitch plane. These results are shown in Figure 6.3 and Figure 6.4 at low speed and high speed, respectively. Additionally, Equations 6.5 to 6.9 describe the closed-loop transfer function for the depth/pitch plane where notations are obvious.

$$\frac{\delta_{elevator}(s)}{Z_{cmd}(s)} = \frac{K_{ZP}K_{\theta P}K_{qp}s[s^3 - (A_{11} + A_{22})s^2 + (A_{11}A_{22} - A_{21}A_{12} - A_{24})s + A_{11}A_{24} - A_{14}A_{21}]}{s^4 + h_1s^3 + h_2s^2 + h_3s + h_4} \quad (6.5)$$

where

$$h_1 = k_{qp}b_2 - (A_{11} + A_{22}) \quad (6.6)$$

$$h_2 = A_{11}A_{22} - A_{21}A_{12} - A_{24} + K_{qp}b_2(K_{\theta P} - A_{11}) + K_{qp}b_1(A_{21} + K_{ZP}K_{\theta P}) \quad (6.7)$$

$$h_3 = K_{\theta P}K_{qp}(A_{21}b_1 - A_{11}b_2) + K_{ZP}K_{\theta P}K_{qp}(A_{12}b_2 - A_{22}b_1 + A_{34}b_2) \quad (6.8)$$

$$h_4 = K_{ZP}K_{\theta P}K_{qp}[(A_{14} - A_{34}A_{11})b_2 + (A_{34}A_{21} - A_{24})b_1] \quad (6.9)$$

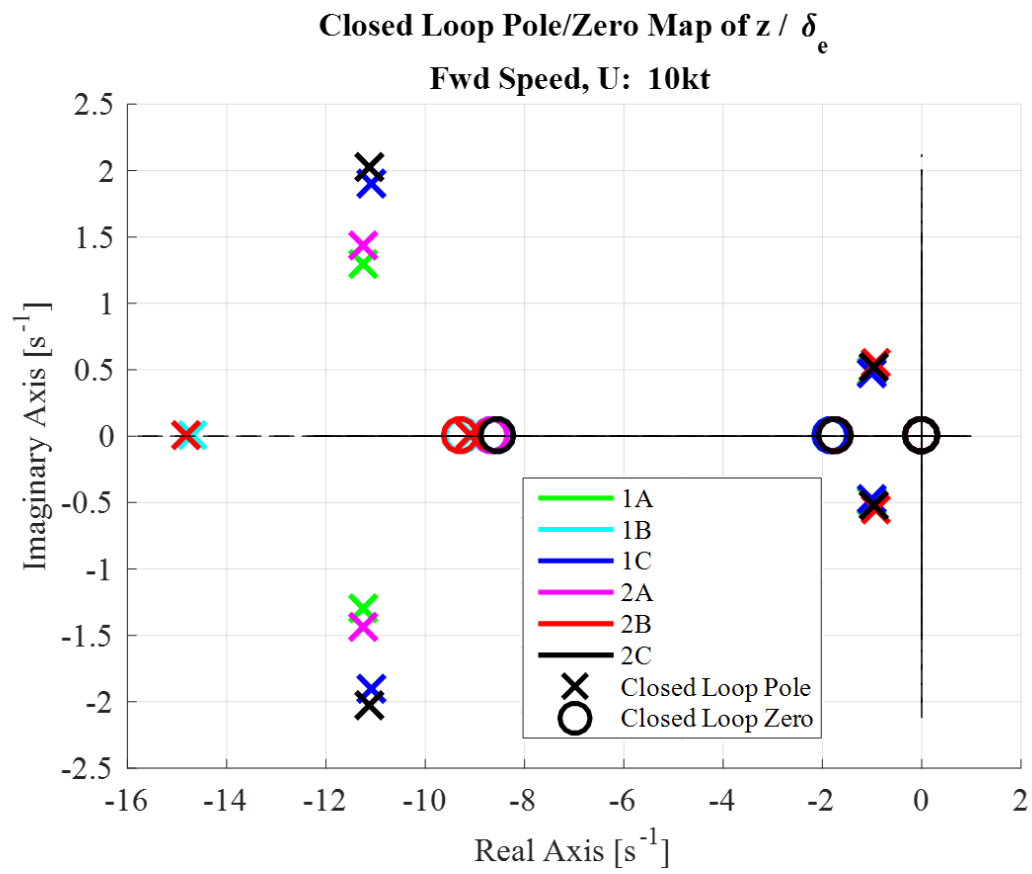


**Figure 6.3. Depth Plane Closed-loop Eigenvalue Clustering, Low Speed**



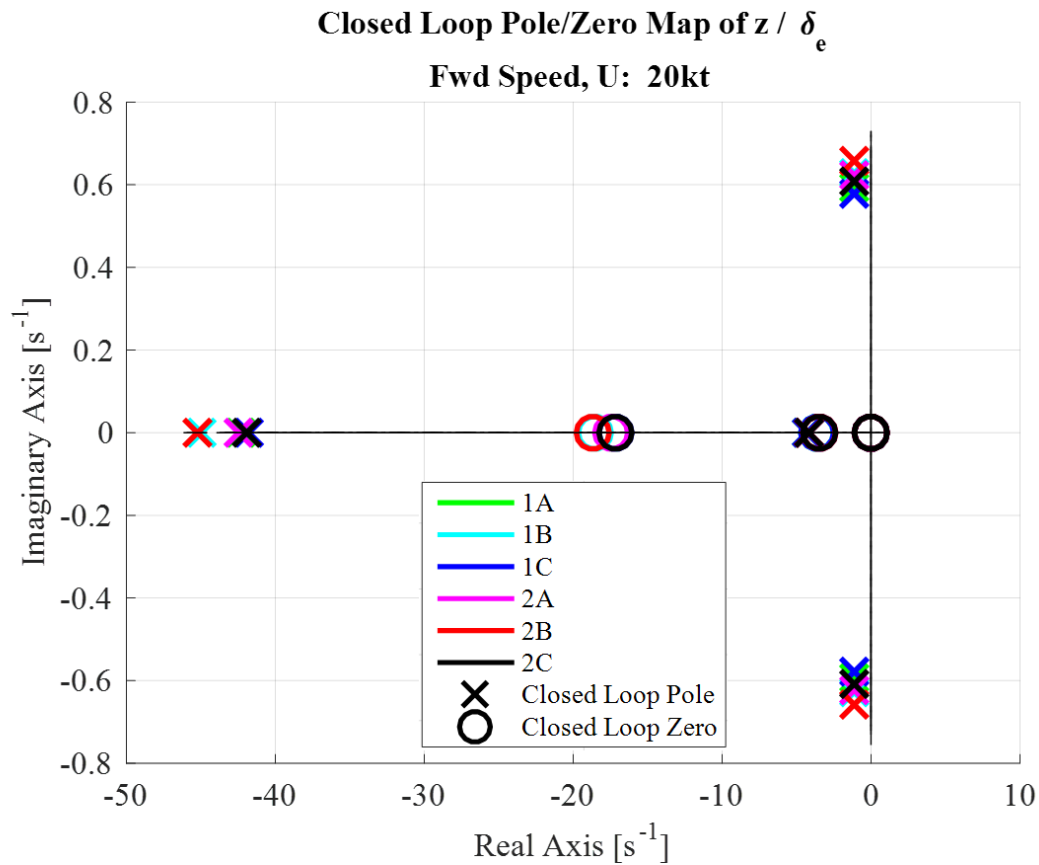


**Figure 6.4. Depth Plane Closed-loop Eigenvalue Clustering, High Speed**

At low speed, there exists two oscillatory modes in the depth/pitch plane. The second oscillatory mode of higher natural frequency only occurs at low speed for weight configurations 1A, 1C, 2A, and 2C. For this particular mode, lower damping characteristics are observed for weight configurations 1C and 2C where the center of mass is offset by one percent of the vehicle length behind the center of buoyancy. Above 17 knots forward speed, the second oscillatory mode becomes critically damped. A nonlinear change in the magnitude of the controller gains for the depth/pitch plane to maintain stability and desired performance contributes to this result. The lower frequency oscillatory mode exists across all speeds maintaining very similar damping and natural frequency characteristics. Although the variations are small, the weight configurations perturbed

furthest from the baseline configuration, 1A, exhibit slightly increased oscillatory behavior. One exception is configuration 1B which exhibits a very slight decrease in oscillatory behavior of the lower frequency oscillatory mode. These two oscillatory modes in the depth/pitch plane can be likened to the well-known short-period and phugoid modes in aircraft dynamics and control as described in [17]. Phugoid modes in longitudinal dynamics of flight vehicles are typically close to the origin, lightly damped, and represent the transitioning of kinetic to potential energy of the system. Short period modes typically vary in distance from the origin and exhibit reasonable damping characteristics. In the case of this study, the short period-like mode becomes critically damped at the high operational speeds of the vehicle.

### 6.2.3 Yaw Plane

The closed-loop eigenvalue clusters of the yaw plane exhibit very similar characteristics to those in the depth/pitch plane due to the symmetry of the UV demonstration vehicle as seen in Figure 6.5 and Figure 6.6. For reference, Equations 6.10 to 6.13 described the closed-loop transfer function for yaw plane where notations are obvious.

$$\frac{\delta_{rudder}(s)}{\psi_{cmd}(s)} = \frac{K_{\psi P} K_{rp} s(s^2 - (A_{11} + A_{22})s + (A_{11}A_{22} - A_{21}A_{12}))}{s^3 + h_1 s^2 + h_2 s + h_3} \quad (6.10)$$

where

$$h_1 = K_{rp} b_2 - (A_{11} + A_{22}) \quad (6.11)$$

$$h_2 = A_{11}A_{22} - A_{21}A_{12} + K_{rp}(A_{21}b_1 - A_{11}b_2) + K_{\psi P} K_{rp} b_2 \quad (6.12)$$

$$h_3 = K_{\psi P} K_{rp} (A_{21}b_1 - A_{11}b_2) \quad (6.13)$$

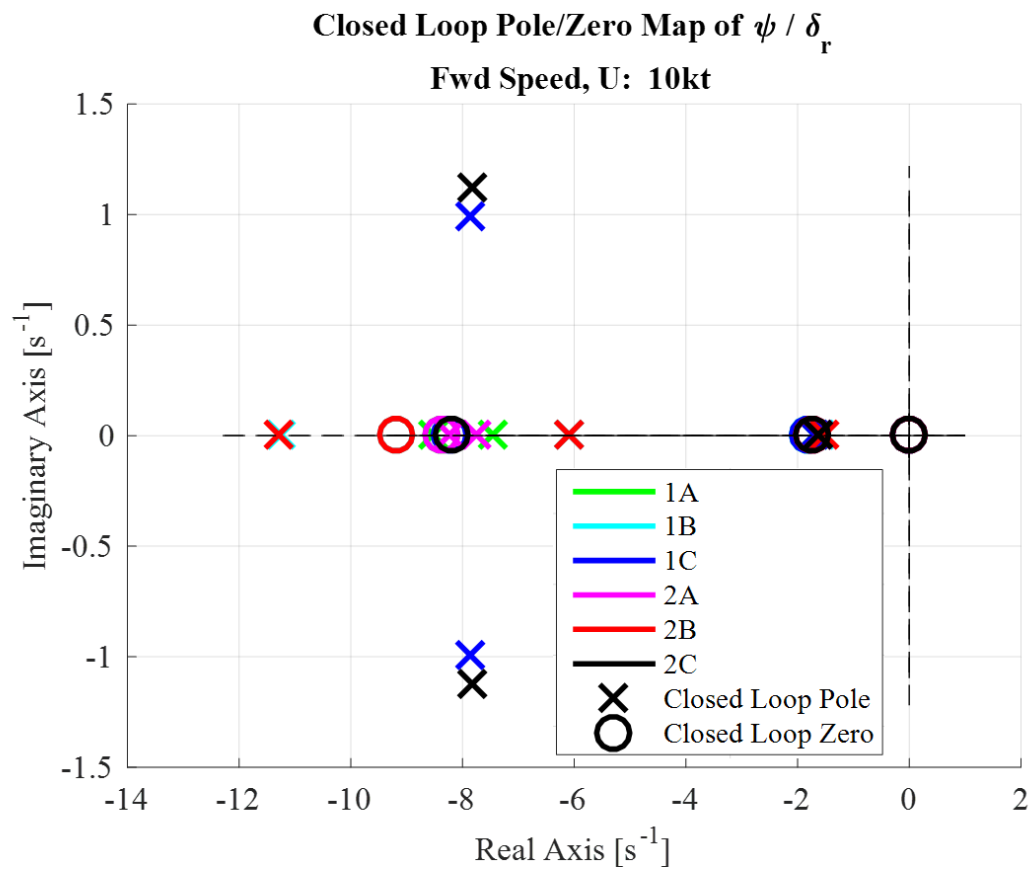


**Figure 6.5. Yaw Plane Closed-loop Eigenvalue Clustering, Low Speed**

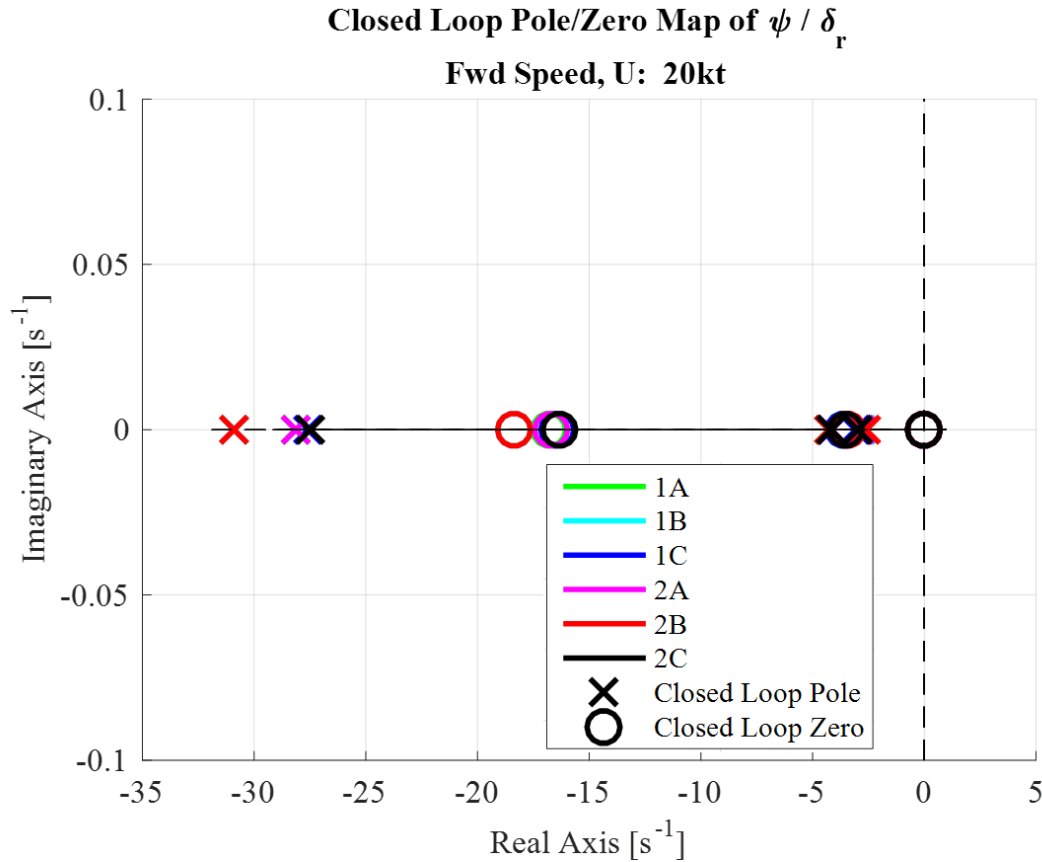


**Figure 6.6. Yaw Plane Closed-loop Eigenvalue Clustering, High Speed**

Compared to the depth/pitch plane, the closed-loop eigenvalues of the yaw plane have generally smaller natural frequencies and some increased damping. Also, the lightly damped oscillatory mode close to the origin in the depth plane is now nonexistent and critically damped in the yaw plane, thereby supporting the notion that there is typically no phugoid mode in lateral flight dynamics. As with the depth/pitch plane, an oscillatory mode does exist further away from the origin at low speeds in the yaw plane and above 18 knots forward speed, this oscillatory mode becomes critically damped. A nonlinear change in the magnitude of the controller gains for the depth/pitch loop to maintain stability and desired performance contributes to this result. As seen in the plots, only small changes in the closed-loop eigenvalue locations of the yaw plane occur for

differing UV weight configurations suggesting that the performance in a UV's lateral dynamics is uninfluenced.

#### **6.2.4 Summary of Eigenvalue Analysis**

In summary, the eigenvalue analysis plots suggest that the baseline, fixed vehicle weight configuration autopilot produces very similar closed-loop eigenvalue locations even when weight configuration changes are made to the UV model. Only minimal variations in eigenvalue locations resulted from the perturbed weight configurations. However, these small variations in eigenvalue locations suggest that flight performance of the UV is impacted. These impacts will be examined in the following sections which discuss the nonlinear flight maneuvering simulation results.

### **6.3 Flight Maneuvering Simulation Analysis**

To further study the robustness of the baseline, fixed vehicle weight configuration autopilot, the nonlinear flight control maneuvering simulation is utilized. Moreover, evaluation of UV flight performance can be well-established through the means of a steady level flight assessment, a steady turn assessment, and a steady depth change assessment. Additionally, the performance of the vehicle must be evaluated at low speed and high speed to fully cover the range of capability of the vehicle. These three assessments of UV flight performance are highlighted in Table 6-1. Note that  $L$  is the length of the UV in meters. Each perturbed weight configuration model outlined in section 2.2 and Table 2-2 is simulated using the same baseline autopilot for each flight performance evaluation.

**Table 6-1. Undersea Vehicle Standard Flight Performance Evaluations**

<b>Flight Performance Evaluation</b>	<b>Metrics of Interest</b>
Steady Level Flight	Trim Angle and Control Surface Deflections
Steady Turn (90 degrees)	Rate Response and Angle Overshoot
Steady Depth Change (3L)	Depth Overshoot

As discussed in Chapter 5, the nonlinear simulation requires a mission command sequence as an input. This mission command sequence dictates the maneuvers that the UV is supposed to perform. Table 6-2 shows an example of what the mission command sequence input file contains for a steady turn flight performance evaluation example. Additionally, each flight performance evaluation mission command sequence can be found in Appendix D. As seen in Table 6-2, the vehicle is commanded to fly steadily at high speed for 10 seconds, turn 90 degrees to the left and hold that angle for 25 seconds until steady state is achieved, turn 90 degrees rightward back to zero and again hold that angle for 25 seconds while steady state is achieved, slow down to slow speed, and complete a similar right-left turning sequence at slow speed. Note that the RPM of the propulsor is directly proportional to the speed of the vehicle. Recall that the commands to each loop of the autopilot are roll angle, depth, and yaw angle in the roll axis, depth/pitch plane, and yaw plane, respectively. Hence, the pitch rates, yaw rates, and pitch angles within the mission command sequence represent the maximum rate and angle limit capabilities for the 12.75 inch diameter UV demonstration model. These turn rate capabilities were determined using best engineering practices based on knowledge of the vehicle body and control surface hydrodynamic characteristics. The pitch angle, set to 45 degrees, is typically the maximum feasible body pitch angle allowable in many UV applications.

**Table 6-2. Mission Command Sequence for Steady Turn Evaluation**

Duration (s)	Roll Angle (deg)	Depth (m)	Pitch Angle (deg)	Pitch Rate (deg/s)	Yaw Angle (deg)	Yaw Rate (deg)	Propulsor RPM
10	0	50	45	66	0	66	1140
25	0	50	45	66	-90	-66	1140
25	0	50	45	66	0	66	1140
40	0	50	45	33	0	33	570
45	0	50	45	33	90	33	570
45	0	50	45	33	0	-33	570

### 6.3.1 Steady Level Flight Simulation Results

The first evaluation produced from the nonlinear flight maneuvering simulation tests steady level flight performance of the UV. By simulating straight-line, rectilinear flight, the trimmed flight angles and control surface deflections are determined. Trim is typically a term designated for quasi-steady flight conditions. In this setting, trimmed conditions are referring to the body angles and control surface deflections observed in steady level flight. To observe autopilot robustness, the baseline, fixed weight configuration autopilot is used by each perturbed weight configuration model. Furthermore, each model is evaluated using the same mission command sequence for steady level flight at 50m depth. The mission command sequence used for steady level flight begins at high speed (20kt) and then transitions to low speed (10kt). Results of the steady level flight simulations can be seen in Figure 6.7 and Figure 6.8. Figure 6.7 shows the speed and depth responses of the vehicle while Figure 6.8 shows the elevator deflection, body pitch angle, and body pitch rate responses. It is important to note that control surface deflection responses correlate identically to the commanded deflections from the autopilot due to the ideal design of the actuator dynamics. Hence, only the response of the control surface deflections will be shown in all results. As expected, the plots reveal different results for each of the perturbed weight configurations. Notably, each perturbed weight configuration (configurations 1B through 2C) exhibits constant

steady state depth error and slight offsets in forward speed. The neutrally buoyant and mass balanced baseline model (1A) trims as expected with no depth offset. The resulting steady trim angle of attack and elevator control surface deflection for each model can be seen in Figure 6.8. The new trimmed flight characteristics of the perturbed models cause a decrease in the forward speed of the vehicle to maintain steady level flight. The decrease in forward speed is caused by increased parasitic drag as a result of increased trim angles of attack and elevator deflection angles. For the heavier or forward biased weight configurations, the elevator deflection compensates by deflecting more negatively to produce a larger positive pitch angle of the UV body. The opposite

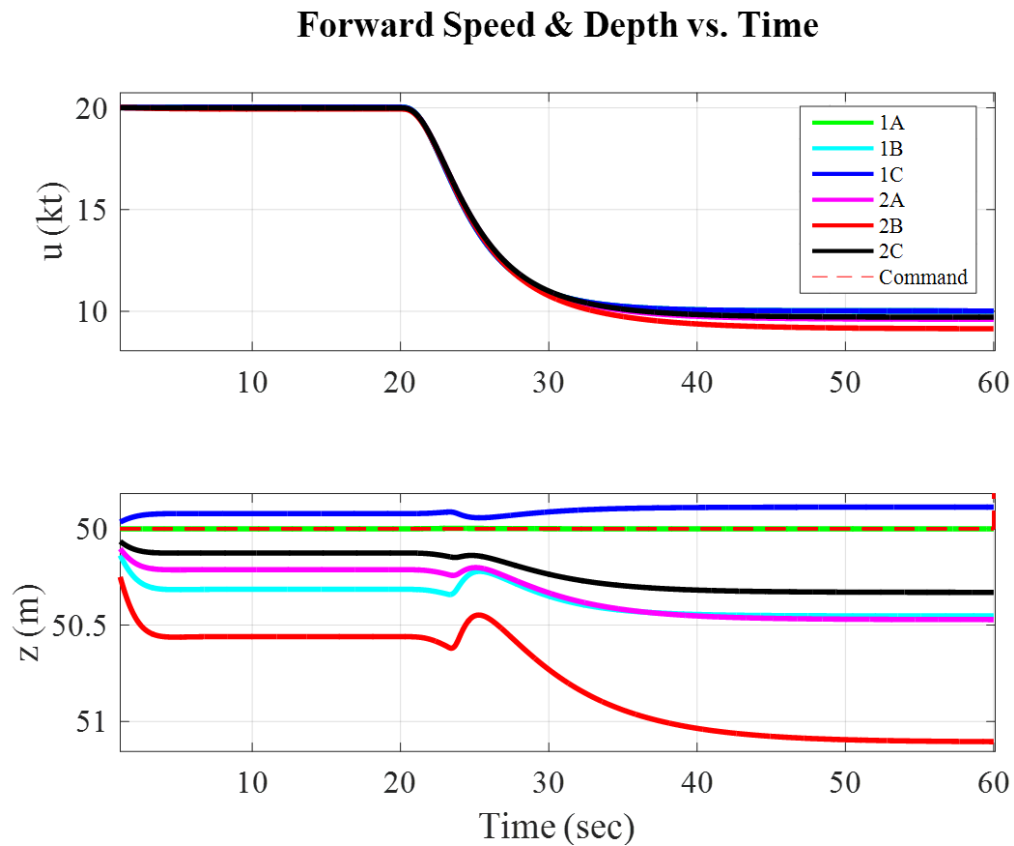


**Figure 6.7. Steady Level Flight: Speed and Depth Responses**



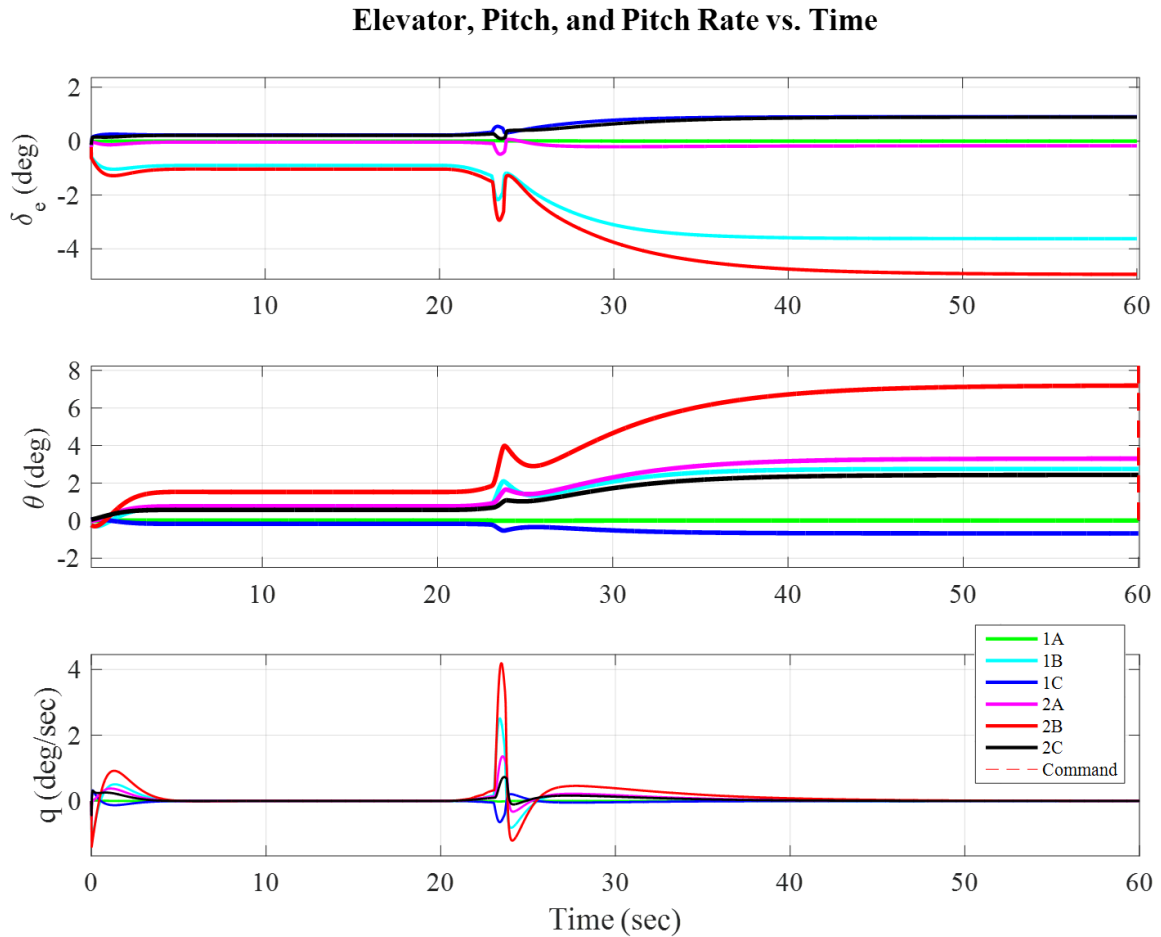


**Figure 6.8. Steady Level Flight: Elevator, Pitch Angle, and Pitch Rate Responses**

is true of configuration 1C, the neutrally buoyant, aft biased weight configuration. A simple force diagram in the vertical plane explaining the steady trim elevator and pitch angles is shown in Figure 6.9. Figure 6.9 shows the major forces acting on the vehicle when maintaining steady flight. The diagram depicts the forces that would be seen for a negatively buoyant, forward weight biased vehicle. A negative deflection angle of the elevator produces a downward force at the tail of the vehicle to pitch the nose of the vehicle upward. Thus, an increased body pitch angle of the vehicle produces an increased lift force on the nose and body to enable the vehicle to maintain steady horizontal flight.

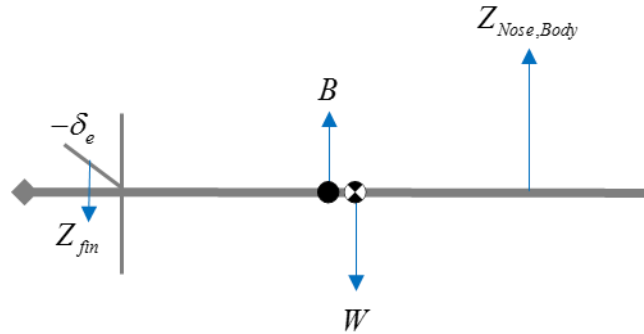


**Figure 6.9. Simple Diagram of Vertical Plane Forces in Steady Level Flight**

The closed-loop eigenvalue plots from section 6.2 suggested that the autopilot would maintain good performance for each perturbed weight configuration. The results from the steady trim simulations support that notion with the exception of the observed depth offset. Steady turn and depth change evaluations in the following sections reveal more about the robustness of the baseline autopilot to changes in vehicle weight configuration.

### 6.3.2 Steady Turn Simulation Results

Steady turn evaluations enable examination of the UV's lateral dynamic responses. For the purposes of this study, a simulation of 90 degree turns at high speed and low speed of the UV demonstration model was performed while maintaining a constant 50m depth command. The results of this simulation are shown in Figures 6.10 and 6.11. Note that the commanded yaw rate resembles the estimated maximum turn rate of the vehicle. Figure 6.10 shows the rudder angle deflection, yaw angle, and yaw rate responses as the vehicle completes the simulated steady turn evaluation mission. The resulting responses of the yaw plane of the vehicle show that variations in weight configuration have very little impact on turning performance of the vehicle. However, the vehicle continues to experience steady state depth error. These errors can be seen in Figure 6.11.

Furthermore, these errors in steady state depth are the same in magnitude as those seen in the steady level flight evaluations. This result makes physical sense as the vehicle is returning to a steady level flight condition after completing a turning maneuver. Hence, the vehicle maintains the same steady level flight characteristics as those seen in the steady level flight evaluations. The baseline autopilot was designed to minimize overshoot and maximize damping and the nonlinear simulation of the vehicle response shows that these characteristics are attained in the yaw plane of motion.

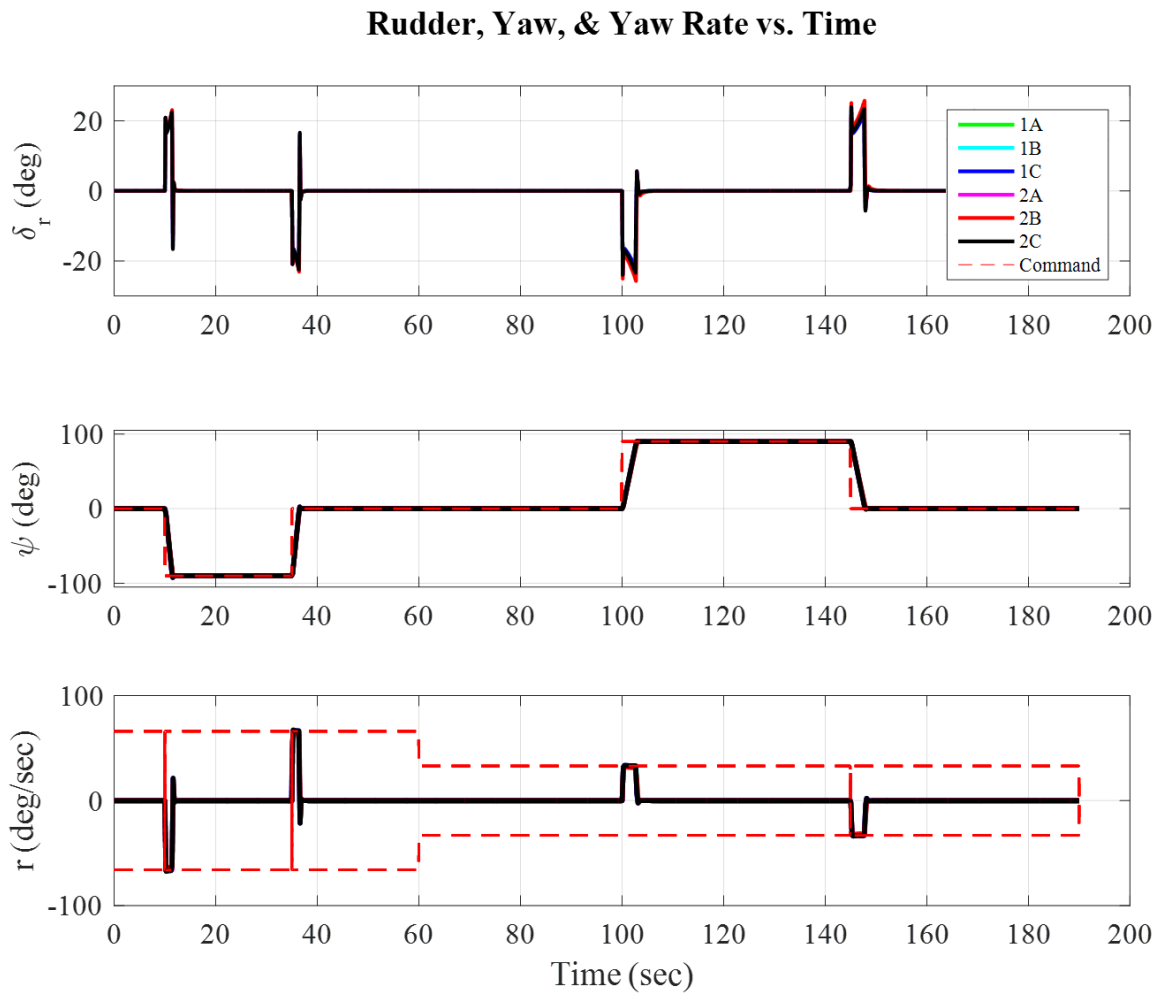


**Figure 6.10. Steady Turn: Rudder, Yaw Angle, and Yaw Rate Responses**

**Forward Speed & Depth vs. Time**

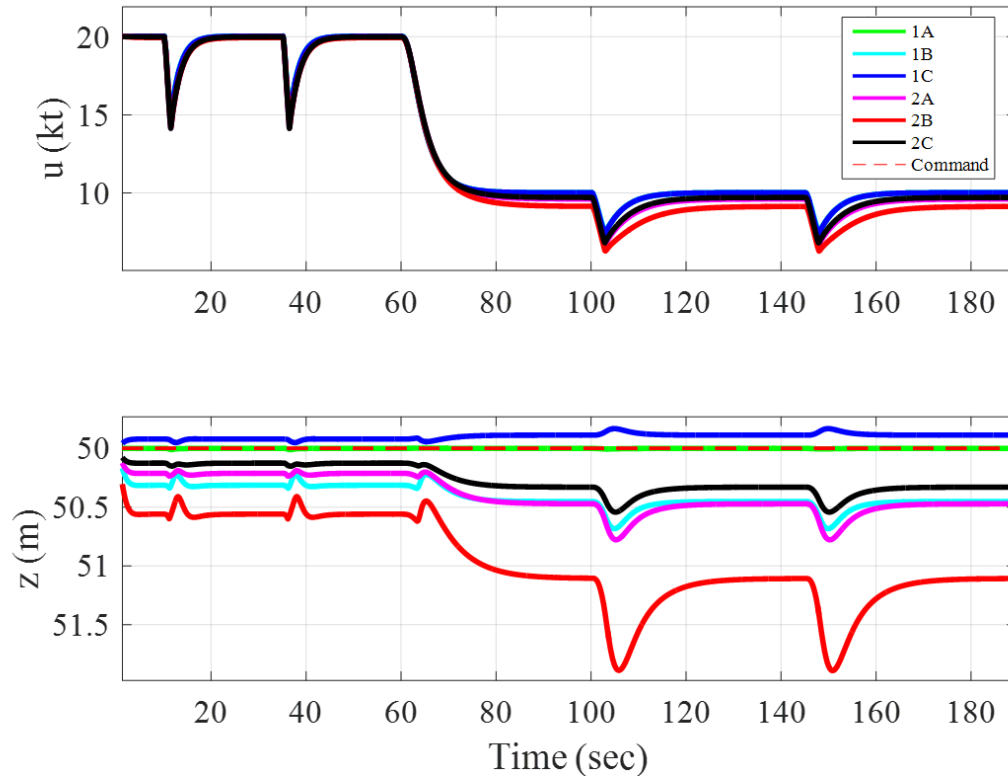


**Figure 6.11. Steady Turn: Speed and Depth Responses**

### 6.3.3 Steady Depth Change Simulation Results

The final flight performance simulation is that of steady depth changes to evaluate depth overshoot. A mission command sequence is used to command depth changes from an initial 50m depth at high speed and low speed. For the purposes of this study, the commanded depth changes were set to three times the overall length of the vehicle or 10.97m. The simulated responses of the vehicle to the steady depth change mission command sequence are shown in Figures 6.12 and 6.13.

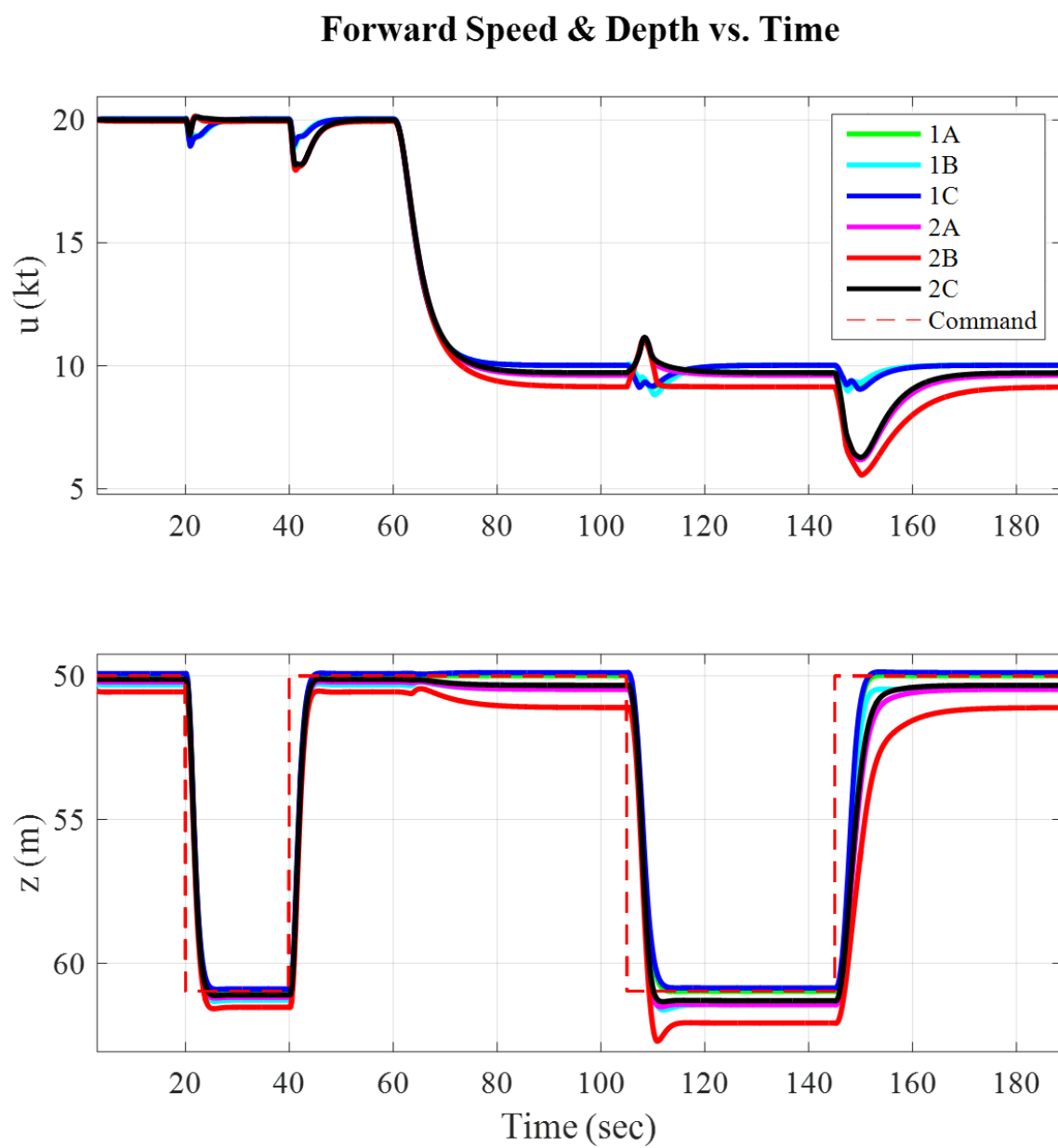


**Figure 6.12. Steady Depth Change: Speed and Depth Responses**

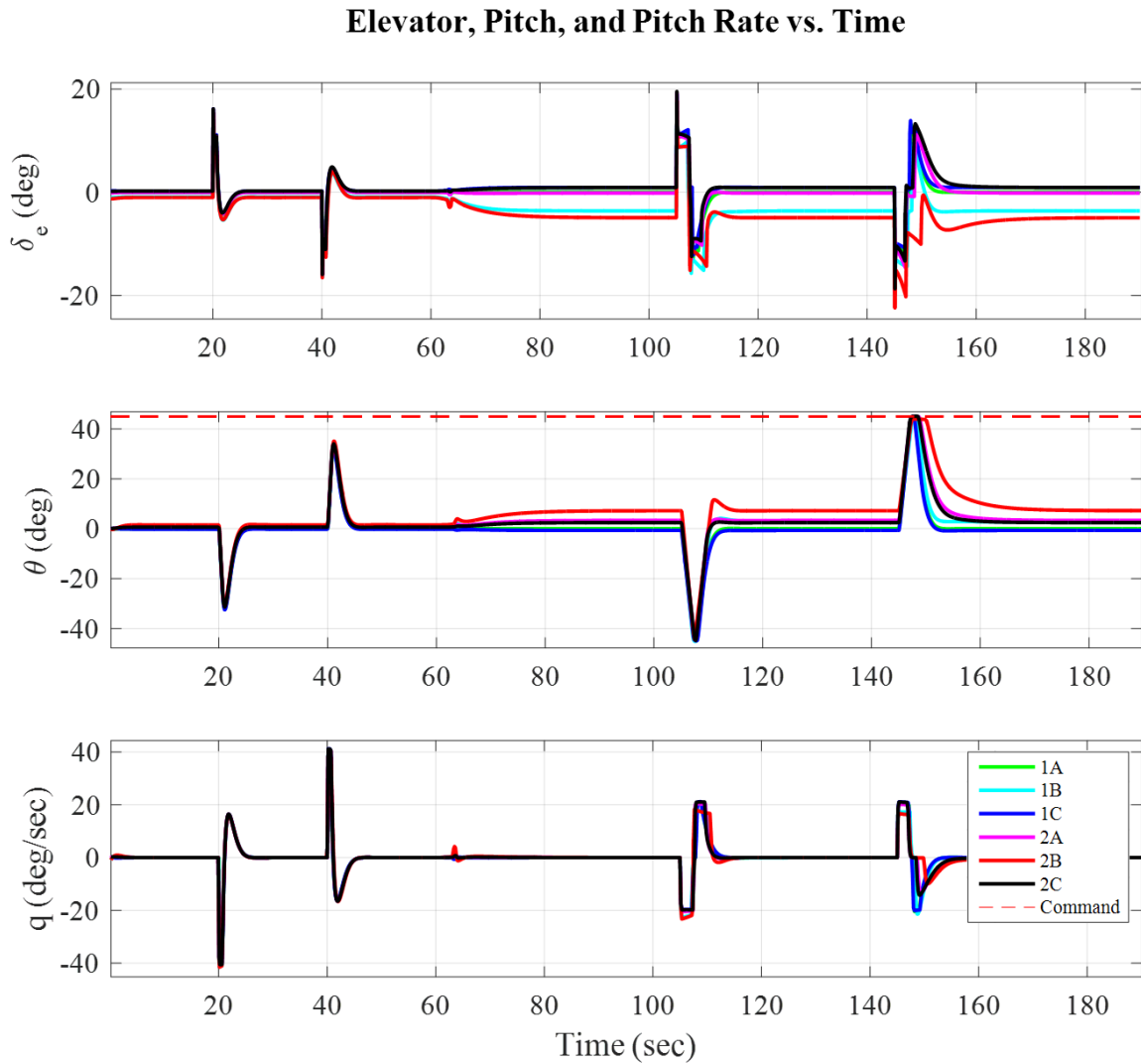


**Figure 6.13. Steady Depth Change: Elevator, Pitch Angle, and Pitch Rate Responses**

The results of the simulated steady depth changes show the robustness of the baseline autopilot to changes in weight configuration of the UV. Minimal depth overshoot is observed for all model responses with the worst cases being configurations 1B and 2B when the vehicle is performing a dive at low speed. Weight configurations 1B and 2B represent the worst case perturbation in center of mass offset being four percent forward of the center of buoyancy of the vehicle. Once again, the same depth error offsets seen in the steady level flight and steady turn simulations are observed

here in the depth change simulation during the steady flight periods of the mission. For a heavier weight configuration, meaning a decrease in effective buoyancy, the vehicle sinks to a deeper depth than desired as it naturally settles to the new trim angle of attack and elevator deflection angle. The same is true of forward weight biased configurations, or the configurations which cause the center of mass to be shifted forward of the center of buoyancy of the vehicle. For the opposing configurations in weight and center of mass locations in which the vehicle is lighter or the center of mass location is shifted aft of the center of buoyancy, the vehicle rises in the water to a shallower depth than desired. Ultimately, the baseline autopilot designed for the original weight configuration, 1A, is compensating for the perturbations in vehicle weight and center of mass locations to reach a new trimmed flight conditions to maintain steady horizontal flight paths, but at the cost of steady state error in depth. Moreover, if the forward speed and weight configuration of the vehicle is held constant, the observed steady state error between commanded and actual attained depth remains constant for any depth command. In other words, the resulting steady state depth error depends on the forward speed and weight configuration of the vehicle. Finally, Figure 6.14 shows a graphical depiction of each weight configuration and observed steady state error in depth at low speed. The steady state depth errors are largest in magnitude at the low operating speed of the vehicle (10kt). Thus, Figure 6.14 shows the worst case magnitudes in state depth error for the prescribed weight configurations and known operational speed range of the vehicle.

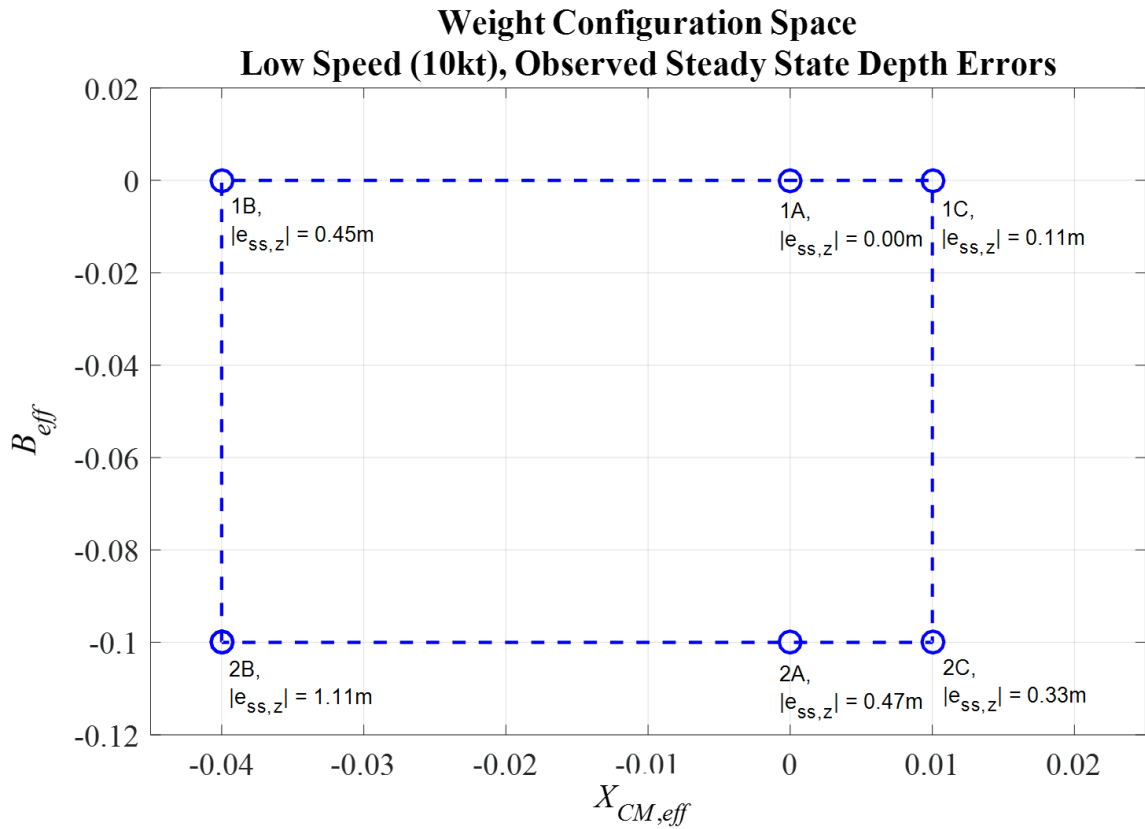


**Figure 6.14. Graphical Depiction of Observed Steady State Depth Errors for Each Vehicle Weight Configuration at Low Speed (10kt)**

#### 6.4 Summary

The results of the prescribed flight performance assessment for UV autopilot robustness were presented in this chapter. Specifically, varying UV weight configurations have little impact on the location of closed-loop poles in the roll axis, depth/pitch plane, and yaw plane. However, the small variations observed on the eigenvalue plots suggested that there would be some difference in flight performance. This suggestion was true as flight performance was evaluated via steady level flight, steady turn, and steady depth change mission command sequences. Although the baseline autopilot is able to successfully maintain reasonable flight performance characteristics in all directions of motion when weight configurations changes are made to the vehicle, steady state



depth error is always observed. The combination of the baseline autopilot and a perturbed weight configuration causes the vehicle to naturally settle to a new steady flight trim condition to maintain a constant horizontal flight path. However, a steady state depth error results for the perturbed vehicle weight configuration models due to a lack of control compensation. Further observations and discussions on offset compensations to remove this depth offset will be discussed in the next chapter.

## Chapter 7

### DISCUSSIONS & OBSERVATIONS

#### 7.1 Governing Rules of Baseline Autopilot Robustness

The results of a prescribed flight performance assessment for undersea vehicle autopilot robustness were presented in the previous chapter. Moreover, the results showed that a well-tuned baseline autopilot maintains robust performance in all directions of motion when unforeseen changes in weight configuration are made. The results suggest that for the specified range of unforeseen changes in a UV's weight configuration, a well-tuned baseline autopilot will maintain reasonable performance. However, undesirable error in steady state depth was observed in each simulation of a perturbed vehicle weight configuration model as a result of new vehicle trim characteristics for maintaining a steady horizontal flight path. Additionally, poor changes in weight configuration of a UV can lead to depth overshoot. Without any compensation, inaccurate control could lead to ineffective mission execution. To that end, an offset compensation, discussed in the following section, can be applied to the desired depth command to effectively eliminate the depth error offset observed at steady flight conditions.

#### 7.2 Offset Depth Compensation and Results

As introduced in the previous section, a baseline autopilot maintains reasonable flight performance robustness to weight configuration changes but at the cost of steady state depth error. An offset compensation on the depth command to the autopilot can be applied to effectively remove the error between desired depth and the newly attained depth by the vehicle. A plot explaining this can be seen in Figure 7.1 showing depth command compensation applied to the worst case

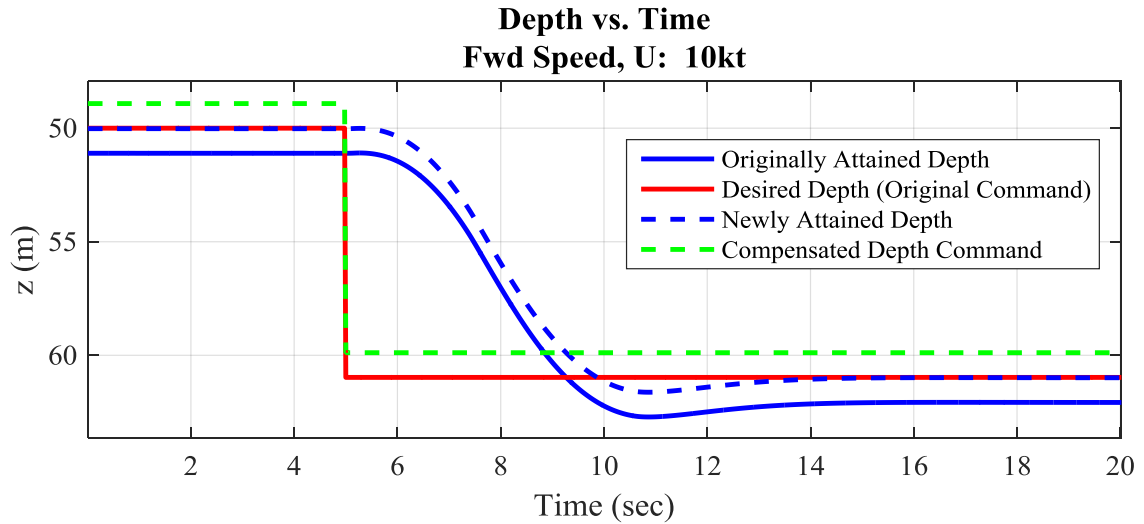


**Figure 7.1. Offset Depth Command Compensation for Configuration 2B**

negatively buoyant and unbalanced weight configuration, 2B, of the generic UV demonstration model at low speed (10kt). The desired depth change shown in Figure 7.1 is the same as the standard three vehicle lengths change in depth used for the simulations presented in section 6.3.3. As seen in the diagram, error exists between the desired depth (original command) and the originally attained depth. Error also exists between the compensated depth command and the newly attained depth. To clarify, the actual steady state error resulting from the dynamic response of a compensated depth command is not removed. However, the newly attained depth matches the desired depth for the mission. Thus, the compensated depth command effectively eliminates the error between the desired depth and the newly attained depth by the vehicle.

The compensation needed on the depth command is scalable with the vehicle weight configuration and forward speed of the vehicle. Based on the observed results of this research, if the forward speed and weight configuration of the vehicle is held constant, the observed steady state error between commanded and actual attained depth remains constant for any depth command.

Finally, it is important to note that the scaling of the compensation needed for the depth command as forward speed of the vehicle changes is not linear.

For a typical range of unforeseen changes to the weight configuration of a vehicle, appropriate compensations can be predetermined to reach desirable depths throughout a mission. Specifically, when utilizing a compensated depth command unique to each perturbed weight configuration and forward speed of the vehicle, the vehicle is able to achieve an originally desired depth. Figures 7.2 and 7.3 show the results of the exact same steady depth change flight performance evaluation as in section 6.3.3 but with compensation gains applied to the depth commands. The compensation gain needed for each perturbed model at each speed is determined by using the observed steady state error for a given speed and weight configuration of the vehicle seen in section 6.3.3. From the observed results in section 6.3.3, the value of the steady state error, or the difference in value between a commanded depth and an actual attained steady state depth, is the same for a given speed and weight configuration of the vehicle. Thus, the compensation gain needed to attain any desired depth for a given constant speed and weight configuration is equivalent to the ratio of the desired depth to the sum of the desired depth and the observed steady state error for that speed and weight configuration. Equation 7.1 shows the computation of the necessary compensation gain needed for a given forward speed and vehicle weight configuration based on the observed steady state error in depth,  $e_{ss,z(obsv)}$ , seen in the results of section 6.3.3.

$$z_{cmd,gain} = \frac{z_{desired}}{z_{desired} + e_{ss,z(obsv)}} \quad (7.1)$$

For example, when commanded to 50m depth at low speed, vehicle weight configuration model 2B attains 51.1m depth at steady state. Thus, by applying a depth compensation gain,  $z_{cmd,gain}$ , equivalent to the ratio of 50:(50+1.1), or 0.9785, to the original 50m depth command, the compensated depth command is determined. Note that the value of the steady state error could be

positive or negative. This same process was repeated for each perturbed model to determine the compensated depth command needed at high speed and low speed at each desired depth of the mission. Moreover, a set of depth compensation gains used for the standard depth change evaluations of the generic UV model can be found in Appendix D.

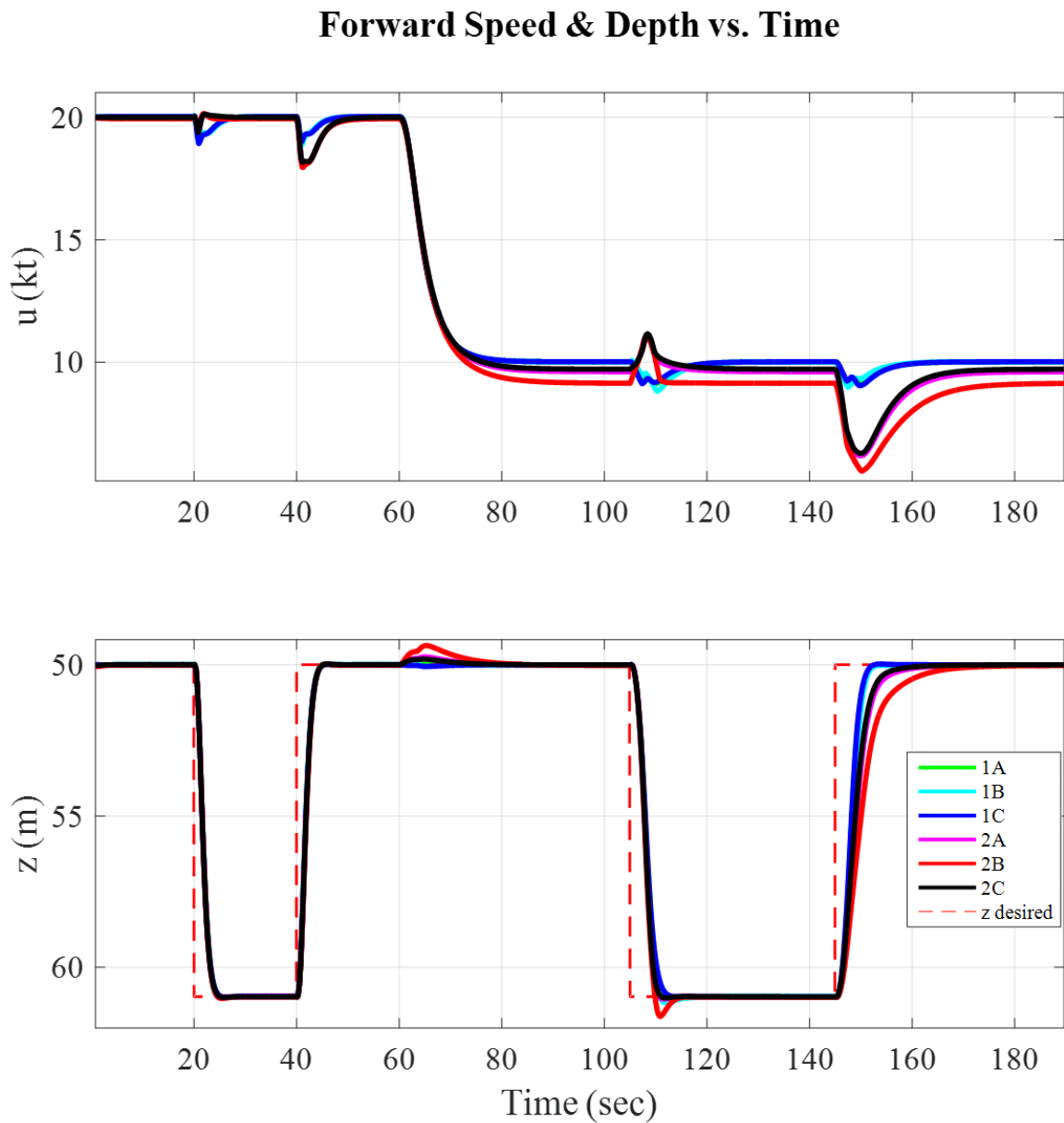


**Figure 7.2. Speed and Depth Responses with Depth Command Compensation**

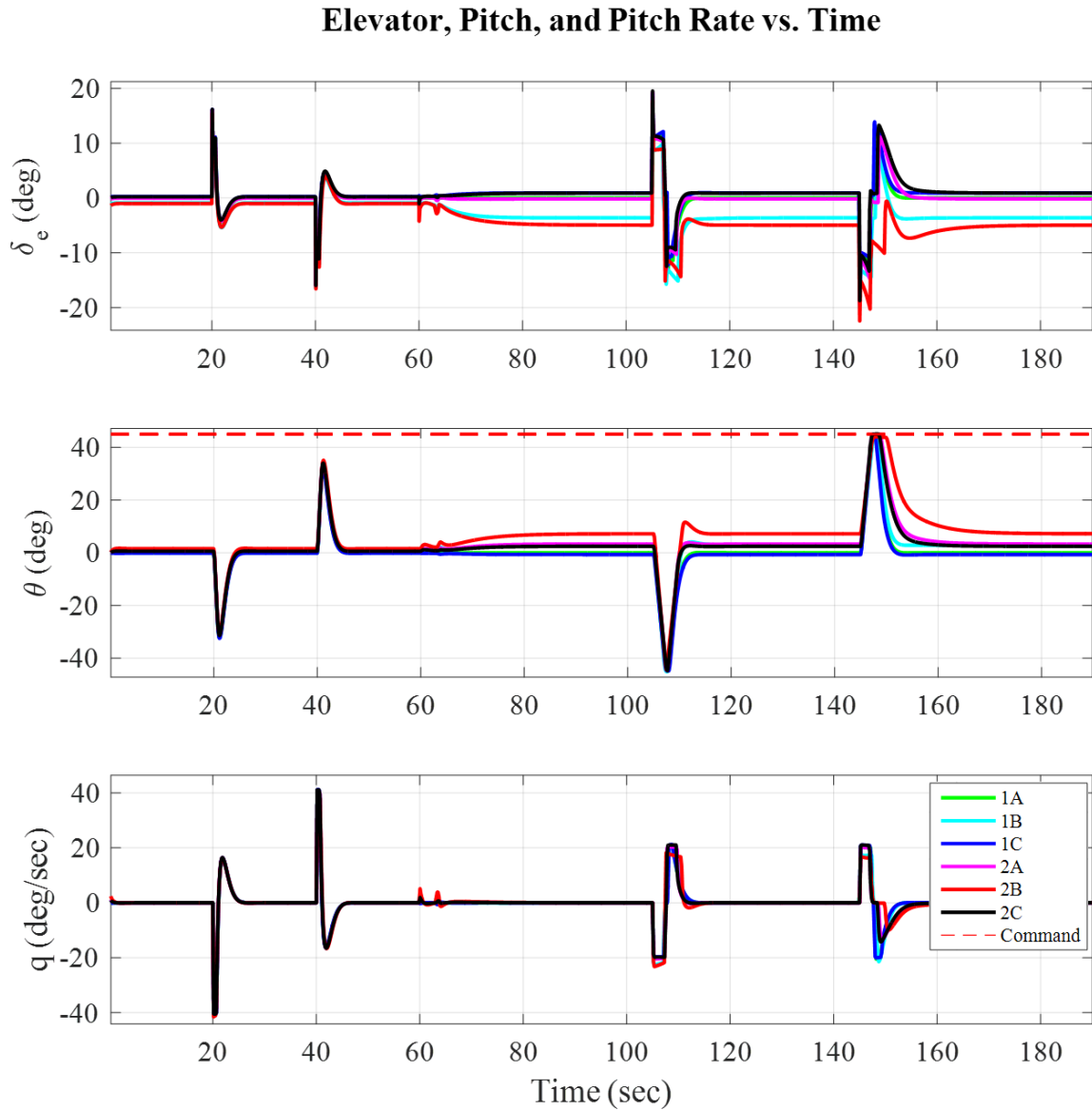


**Figure 7.3. Elevator, Pitch, and Pitch Rate Responses with Depth Compensation**

Figure 7.3 shows the resulting responses of the vehicle elevator deflection, pitch angle and pitch rate. The elevator deflection and pitch angle responses in Figures 7.3 and 6.13 are very similar. As expected, the steady state trim elevator deflections and pitch angles at high speed or low speed are the same for each weight configuration regardless of whether or not compensation is performed on the depth command. This result makes sense because each perturbed weight configuration model

is remaining unchanged, the order of each model is remaining unchanged, and the baseline autopilot and its gains are remaining unchanged. Thus, the baseline autopilot and perturbed weight configuration vehicle model combinations naturally settle to new trimmed angles of attack and elevator deflections. Also, the new trimmed conditions lead to decreased forward speed of the vehicle due to parasitic drag effects.

The compensated depth command represents the compensation that a retuned autopilot would need to adopt as a result of new steady level flight trim characteristics of a perturbed vehicle weight configuration. The baseline autopilot was designed for the baseline vehicle configuration and baseline trim conditions, thereby, limiting its ability to control the vehicle to desirable depths when weight configuration changes are made to the vehicle. Furthermore, the baseline vehicle weight configuration is neutrally buoyant and evenly mass distributed. Thus, the baseline autopilot was designed for steady level flight trim characteristics consisting of zero body pitch angle and zero elevator deflection. However, each perturbed weight configuration model exhibits differing steady level flight trim characteristics. A compensated depth command to the autopilot produces slightly different commands at each stage (depth, pitch, and pitch rate) of the autopilot at the time of the command to achieve the desired depth. To summarize, the compensated depth command translates to the compensation needed within each loop of the depth/pitch plane controller to accommodate the new equilibrium trim characteristics of the vehicle to achieve a desired depth and maintain horizontal steady level flight.

The differences in elevator deflection produced by the compensated depth commands are very small when comparing the results within Figure 6.13 and Figure 7.3, but without this small difference the vehicle cannot attain the desired depth. To visually show that the elevator deflection angle is indeed changing due to changes in depth command, Figure 7.4 shows the vehicle responses to a five meter depth change and a 10 meter depth change. Each simulated response is that of the worst case negatively buoyant and unbalanced weight configuration, 2B, of the generic UV

demonstration model. The five meter depth changes are between 30 and 35 meter depths at high and low speed while the 10 meter depth changes are between 50 and 60 meter depths at the same speed and time of transition. Furthermore, compensated depth commands were utilized in this simulation to achieve the desirable 30, 35, 50, and 60m depths illustrating successful compensation on the depth commands to reach desirable depths different from those previously shown.

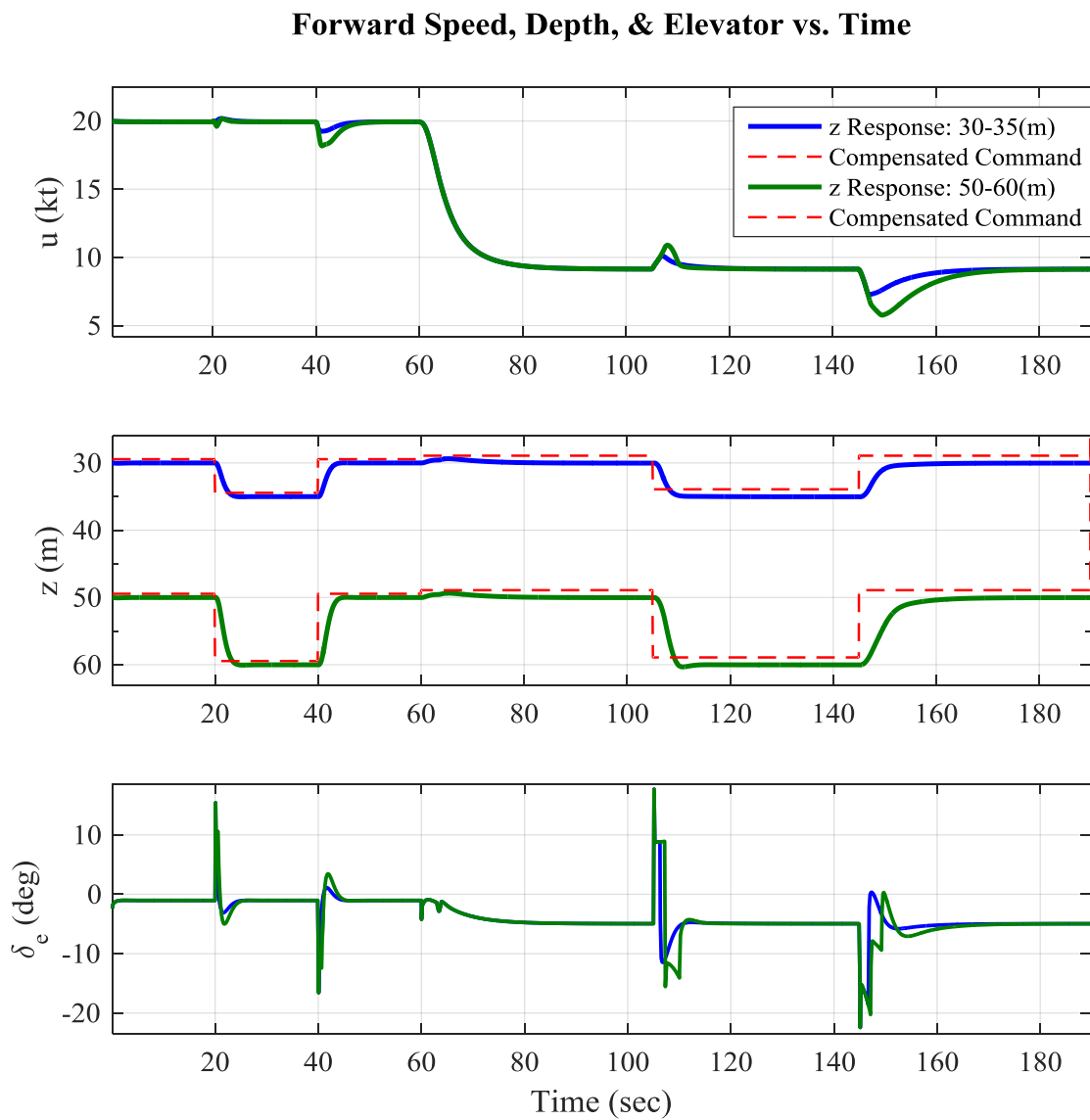


**Figure 7.4. Five and Ten Meter Depth Change Evaluations with Depth Compensation**



### 7.3 Summary

To summarize, the baseline fixed weight configuration autopilot is capable of maintaining reasonable performance in all planes and axes of motion when perturbations in weight configuration are made to the vehicle. Although relatively good performance is maintained, the perturbed weight configurations do cause steady state depth error. The observed steady state depth error is a result of the perturbed vehicle weight configuration and baseline autopilot combination naturally settling to a new steady dynamic equilibrium state, or trim. The weight configuration differences result in new elevator deflection and pitch angle trim conditions to maintain a steady horizontal flight path. A constant horizontal flight path is dictated by a constant depth command to the autopilot. Thus, the perturbed weight configurations lead to new vehicle trim characteristics to maintain steady horizontal flight, but steady state depth error results from a lack of compensation within the depth/pitch plane controller. Furthermore, to achieve desirable depths without retuning the autopilot, an offset depth compensation can be applied to the depth command into to the autopilot to eliminate the observed error in steady state depth. By applying a compensation gain to the desired depth command that is unique to the weight configuration and forward speed of the vehicle, the baseline autopilot is able to control the vehicle to the desired depth.

## Chapter 8

### CONCLUSIONS & RECOMMENDATIONS

#### 8.1 Conclusions

In many undersea vehicle applications unplanned or unforeseen changes to the vehicle weight configuration do occur. These changes often include vehicle mission payload weight and vehicle mass distribution. An example related to this research effort is an unplanned replacement of a UV payload by a heavier or lighter payload. Moreover, when these unforeseen changes occur, a full autopilot re-design cycle is typically not possible or straight forward. Ultimately, the unplanned changes in weight configuration to a UV can lead to an ineffective mission execution. The purpose of this research was to establish and outline a prescribed flight performance assessment for undersea vehicle autopilot robustness. Furthermore, the robustness of a baseline, fixed weight configuration autopilot was tested against variations in two defined non-dimensional parameters, vehicle effective buoyancy,  $B_{eff}$ , and effective center of mass offset,  $X_{CM,eff}$ . The range of perturbations in effective buoyancy and effective center of mass offset were selected for the typical unforeseen changes to weight configurations of operational UVs in service today. Ultimately, the results of the prescribed assessment showed that an original, well-tuned, fixed weight configuration autopilot is capable of maintaining flight performance but at the cost of a steady state depth offset error. The error results from the perturbations in vehicle weight and center of mass location producing new trim conditions of the vehicle to maintain a steady horizontal flight path without any added depth/pitch plane control compensation. However, an offset compensation on the depth command to the autopilot effectively removes the error between the newly achieved depth and the desired (originally commanded) depth. To summarize, the compensated depth command translates to the compensation needed within each loop of the depth/pitch plane

controller to accommodate the new equilibrium trim characteristics of the vehicle to reach a desired depth and maintain horizontal steady level flight. Additionally, the offset compensation applied to the depth command avoids retuning of the autopilot.

Some caution needs to be taken when considering the use of compensated depth commands for changes to a vehicle's weight configuration. There are limits to the available body and fin (control surface) lift components to maintain steady or reasonable angle of attack. In other words, the body geometric properties, low operational speed, and control surface properties of a UV are a few of the key parameters that dictate the maximum change in a UV's weight configuration. For example, if a vehicle is overloaded or the mass is re-distributed to be too far forward, the vehicle will not be able to maintain steady flight at any operating condition. Increasing the low speed of the vehicle can help to maintain operational flight under extreme loading conditions, but ultimately limits to the magnitude of weight configuration changes do exist. Continuing in this regard, an increase in speed within the operating range of the vehicle for any perturbed weight configuration will help increase flight performance. Higher speed leads to increased lift on the vehicle body and control surfaces, thereby, requiring less compensation on the depth commands to attain desired depth. Ultimately, the prescribed assessment presented in the previous chapters can be used to determine the limits of possible changes in vehicle weight configurations that would result in a failed mission execution without a retuned autopilot, increased low speed, or a geometric (hydrodynamic) change to the vehicle.

To summarize, the four key takeaways from this research are the following:

1. A baseline autopilot is robust to changes in a UV's weight configuration,
2. A steady state depth error offset is always observed when a baseline autopilot is used to control a perturbed weight configuration UV as a result of new steady horizontal flight trim characteristics of the vehicle without any added control compensation in the depth/pitch plane,

3. An offset compensation can be applied to a desired depth command to attain the desired depth without retuning the autopilot, and
4. The results of this research are analogous to other original UV weight configurations and baseline autopilots.

Expounding on the above takeaways, a significant outcome of this research is proof of the notion that an originally well-tuned autopilot is able to adequately handle the typically unforeseen changes to a UV's weight configuration. Although the baseline vehicle configuration herein was a neutrally buoyant and weight balanced vehicle, the baseline autopilot handled weight configuration changes within the prescribed range in effective buoyancy and effective center of mass offset. Therefore, the results found here are analogous to what would be seen for any original UV configuration that is perturbed within a similar range of weight configurations. This notion suggests that any original fixed weight configuration UV and its well-tuned baseline autopilot combination would be reasonably robust to changes in the vehicle's weight configuration. Moreover, if the typical unforeseen changes to a UV's weight configuration are known, then the prescribed flight performance assessment presented here can help to determine the required compensations that would be needed to achieve desirable depths. Through the addition of a vehicle weight configuration sensor to a UV to provide measurements of the changes in a vehicle's center of mass location and payload weight, the depth compensations could be made more readily. However, future work would need to investigate analytical or iterative solutions accommodating varying weight configurations and resulting vehicle trim conditions to readily compute the necessary depth compensations from the sensor measurements.

## 8.2 Recommendations

The offset depth compensation on the depth command is scalable to changes in weight configuration and forward speed of the vehicle. Albeit not straight forward, this observation suggests that an analytical or iterative numerical solution exists for the necessary compensation needed on the depth command using steady state error and equilibrium dynamics (trim) analysis. Investigations into the analytical or iterative numerical solution are recommended in future extensions of this research.

As observed in the results, the baseline autopilot reasonably maintains desired flight performance at the cost of a steady state depth error related to differing steady flight trim characteristics including angle of attack and elevator deflection angles. This result indicates that the addition of an integral control component to the outer depth loop control stage of the autopilot depth/pitch control loop would naturally eliminate the observed steady state error. However, the addition of an integral controller increases the order to the closed-loop system complicating the system dynamics. If an integral component were added and incorporated as an original feature of the baseline autopilot, the implications to optimization of minimum overshoot with added integrator dynamics and the implications of the added delay on autopilot optimum performance tuning effects would need to be investigated.

The scope of this research effort did not include the effects of changing the hydrodynamic properties of a UV. Namely, changes in hydrodynamic coefficients which are influenced by geometric changes to the vehicle shell/hull or control surfaces were not investigated. Rather, a study of the typically unforeseen changes to current in-service UV weight configurations was conducted. Additionally, changes to the weight configuration of a UV are decoupled from the hydrodynamic coefficients. Vehicle hulls and control surfaces are typically fixed designs after production. However, the prescribed flight performance assessment presented herein can be further

used to analyze future design configurations involving varying vehicle shell and control fin geometries. Moreover, the eight dominant hydrodynamic coefficients used for basic UV control design,  $M_{uw}$ ,  $M_{uq}$ ,  $Z_{uw}$ ,  $Z_{uq}$ ,  $N_{ur}$ ,  $N_{uv}$ ,  $Y_{ur}$ , and  $Y_{uv}$ , which are highly and complexly coupled to basic changes in UV geometric properties could be varied collectively and flight performance impacts investigated rather than each individual coefficient of a UV or all coefficients of a UV as in [4]. The basic changes in UV geometric properties include length, diameter, axial distance from the nose to CB, axial distance from the nose to center of lift of the tail, nose lift slope, tail lift slope, and planform area of the control surfaces.

## Appendix A

### Glossary of Terms

cg, CM : Center of gravity (Center of mass)  
 CB: Center of Buoyancy  
 $m$ : Mass of vehicle  
 $I_{xx}$  : Mass moment of inertia about body longitudinal axis  
 $I_{yy}$  : Mass moment of inertia about body lateral axis  
 $I_{zz}$  : Mass moment of inertia about body vertical axis  
 $L$ : Length of vehicle  
 $D$ : Diameter of vehicle  
 $A$ : System matrix used for yaw, pitch, and roll  
 $B$ : Control matrix used for yaw, pitch, and roll  
 $B_{uoy}$ : Buoyancy of vehicle  
 $\overline{C}_f, C_f$ : Matrices depicting crossflow  
 $M$ : System mass matrix  
 $W$ : Weight of vehicle  
 $B_{eff}$ : Vehicle effective buoyancy  
 $X_{CM,eff}$ : Vehicle effective center of mass location  
 $X_{CB}$ : Axial distance from nose of the vehicle to the vehicle CB  
 $X_{tail}$ : Axial distance from CB to center of lift at tail of vehicle  
  
 $W_{C_{Dcf}}(x)$ : Function used in crossflow calculations  
 $\delta_s$ : Splay control fin  
 $\delta_r$ : Rudder control fin  
 $\delta_e$ : Elevator control fin  
 $\rho$ : Mass density of sea water  
  
 $u, \dot{u}$ : Linear velocity and acceleration, respectively, along body longitudinal axis  
 $v, \dot{v}$ : Linear velocity and acceleration, respectively, along body lateral axis  
 $w, \dot{w}$ : Linear velocity and acceleration, respectively, along body vertical axis  
 $x, y, z$ : Inertial or earth-fixed coordinates  
  
 $p, \dot{p}$ : Roll rate and acceleration, respectively  
 $q, \dot{q}$ : Pitch rate and acceleration, respectively  
 $r, \dot{r}$ : Yaw rate and acceleration, respectively

$\phi, \dot{\phi}$ : Roll Euler angle and rate, respectively  
 $\theta, \dot{\theta}$ : Pitch Euler angle and rate, respectively  
 $\psi, \dot{\psi}$ : Yaw Euler angle and rate, respectively

$V_t$ : Total velocity at the tail of the vehicle  
 $\phi_t$ : Roll Euler angle at the tail of the vehicle

$\eta$ : Self-propulsion acceleration ratio  
 $\eta_{stator}$ : Efficiency of the stator

$T_{|n|n}$ : Thruster parameter  
 $T_{|n|V_a}$ : Thruster parameter  
 $n$ : Propeller revolution (rev/s)  
 $t_{ded}$ : Thrust deduction  
 $w$ : Wake fraction  
 $J_o$ : Propulsor advance number (1/rev)  
 $D_{prop}$ : Propulsor tip diameter

$Q_{|n|n}$ : Thruster parameter  
 $Q_{|n|V_a}$ : Thruster parameter

$x_g, X_{CM}$ : Center of gravity location along body longitudinal axis measured from center of buoyancy  
 $y_g$ : Center of gravity location along body lateral axis measured from center of buoyancy  
 $z_g$ : Center of gravity location along body vertical axis measured from center of buoyancy

$X_{qq}$ : Centripetal angular pitch velocity axial drag term  
 $X_{rr}$ : Centripetal angular yaw velocity axial drag term  
 $X_{\ddot{u}}$ : Added mass term due to acceleration  $\ddot{u}$   
 $X_{vr}$ : Angular yaw velocity body lift axial drag term  
 $X_{wq}$ : Angular pitch velocity body lift axial drag term  
 $X_{uq\delta_e}$ : Elevator control fin pitch angular velocity axial drag term  
 $X_{uv\delta_r}$ : Rudder control fin yaw angular velocity axial drag term  
 $X_{vv}$ : Lateral linear velocity axial drag term  
 $X_{ww}$ : Normal linear velocity axial drag term  
 $X_{uv\delta_r}$ : Rudder control fin yaw linear lateral velocity axial drag term  
 $X_{uw\delta_e}$ : Elevator control fin pitch linear normal velocity axial drag term  
 $X_{uu\delta_e\delta_e}$ : Elevator control fin quadratic axial drag



$X_{uu\delta_r\delta_r}$  : Rudder control fin quadratic axial drag

$X_{uu\delta_s\delta_s}$  : Splay control fin quadratic axial drag

$X_{uu}$  : Quadratic body axial drag

$Y_{pq}$  : Added mass cross term due to Coriolis acceleration

$Y_{\dot{r}}$  : Added mass due to acceleration  $\dot{r}$

$Y_{\dot{v}}$  : Added mass due to acceleration  $\dot{v}$

$Y_{ur}$  : Angular yaw velocity body lift term

$Y_{ur(\eta-1)}$  : Off self-propulsion angular yaw velocity body lift term

$Y_{wp}$  : Added mass cross term due to Coriolis acceleration

$Y_{uv}$  : Lateral velocity body lift term

$Y_{uv(\eta-1)}$  : Off self-propulsion lateral velocity body lift term

$Y_{uvprop}$  : Propulsor lateral velocity body lift term

$Y_{uu\delta_r\delta_r}$  : Quadratic lateral rudder control fin drag term

$Y_{uu\delta_r(\eta-1)}$  : Off self-propulsion lateral rudder control fin drag term

$Y_{cf}'$  : Crossflow drag coefficient

$Z_{pr}$  : Added mass cross term due to Coriolis acceleration

$Z_{\dot{q}}$  : Added mass due to acceleration  $\dot{q}$

$Z_{\dot{w}}$  : Added mass due to acceleration to  $\dot{w}$

$Z_{uq}$  : Angular pitch velocity body lift term

$Z_{uq(\eta-1)}$  : Off self-propulsion angular pitch velocity body lift term

$Z_{vp}$  : Angular pitch velocity body lift term

$Z_{uw}$  : Normal velocity body lift term

$Z_{uw(\eta-1)}$  : Off self-propulsion normal velocity body lift term

$Z_{uwprop}$  : Propulsor normal velocity body lift term

$Z_{uu\delta_e}$  : Elevator control fin lift term

$Z_{uu\delta_e(\eta-1)}$  : Off self-propulsion elevator control fin lift term

$Z_{cf}'$  : Crossflow drag coefficient

$K_{up}$  : Roll angular velocity drag term

$K_{up(\eta-1)}$  : Off self-propulsion roll angular drag term

$K_{uu(\eta-1)}$  : Off self-propulsion roll term

$K_{uu\delta_s}$  : Splay control fin body lift

$K_{uu\delta_s(\eta-1)}$  : Off self-propulsion splay control fin body lift

$K_{\sin(4\phi)}$  : Control fin roll drag

$M_{rp}$  : Added mass cross term due to Coriolis acceleration  
 $M_{\dot{q}}$  : Added mass term due to pitch acceleration  
 $M_{\dot{w}}$  : Added mass term due to normal acceleration  
 $M_{uq}$  : Angular pitch velocity body lift term  
 $M_{uq(\eta-1)}$  : Off self-propulsion angular pitch velocity body lift term  
 $M_{vp}$  : Added mass term due to Coriolis acceleration  
 $M_{u\delta_s}$  : Splay control fin lift term  
 $M_{uu\delta_e}$  : Elevator control fin body lift term  
 $M_{uu\delta_e(\eta-1)}$  : Off self-propulsion elevator control fin body lift term  
 $M_{uv\delta_s}$  : Splay control fin lateral velocity lift term  
 $M_{uw}$  : Normal velocity body lift term  
 $M_{uw(\eta-1)}$  : Off self-propulsion normal velocity body lift term  
 $M_{uwprop}$  : Propulsor normal velocity body lift term  
 $M'_{cf}$  : Crossflow drag coefficient

$N_{pq}$  : Added mass cross term due to Coriolis acceleration  
 $N_{\dot{r}}$  : Added mass term due to yaw acceleration  
 $N_{\dot{v}}$  : Added mass term due to lateral acceleration  
 $N_{ur}$  : Angular yaw velocity body lift term  
 $N_{ur(\eta-1)}$  : Off self-propulsion angular yaw velocity body lift term  
 $N_{wp}$  : Added mass term due to Coriolis acceleration  
 $N_{uq\delta_s}$  : Splay control fin pitch angular velocity lift term  
 $N_{uv}$  : Lateral velocity body lift term  
 $N_{uv(\eta-1)}$  : Off self-propulsion lateral velocity body lift term  
 $N_{uu\delta_r}$  : Rudder control fin body lift term  
 $N_{uu\delta_r(\eta-1)}$  : Off self-propulsion rudder control fin body lift term  
 $N_{uw\delta_s}$  : Splay control fin normal velocity lift term  
 $N_{uvprop}$  : Propulsor lateral velocity body lift term  
 $N'_{cf}$  : Crossflow drag coefficient

## Appendix B

### Undersea Vehicle Hydrodynamic and Propulsor Model

The values presented in Table B-1 are those of the baseline neutrally buoyant and weight balanced 12.75 inch diameter UV demonstration vehicle model (weight configuration 1A from Table 2-2). Only the dominant hydrodynamic coefficients are listed. All others are zero valued or negligible.

**Table B-1. Generic Undersea Vehicle Hydrodynamic Simulation Model**

Parameter	Value	Units
$L$ :	3.6576	$m$
$D$ :	0.3239	$m$
$m$ :	285.3 (629)	$kg$ (lb.)
$B_{uoy}$ :	285.3 (629)	$kg$ (lb.)
$X_{CB}$ :	1.7587	$m$
$X_{tail}$ :	1.6581	$m$
$x_g, X_{CM}$ :	0.0	$m$
$y_g$ :	0.0	$m$
$z_g$ :	0.0127	$m$
$B_{eff}$ :	0.0	Non-dimensional
$X_{CM,eff}$ :	0.0	Non-dimensional
$I_{xx}$ :	1.5293	$kg \cdot m^2$
$I_{yy}$ :	176.1	$kg \cdot m^2$
$I_{zz}$ :	176.1	$kg \cdot m^2$
$X_{qq}$ :	-24.8072	$kg \cdot m / rad^2$
$X_{rr}$ :	24.8072	$kg \cdot m / rad^2$
$X_{\dot{u}}$ :	-4.9049	$kg$
$X_{vr}$ :	292.3186	$kg / rad$
$X_{wq}$ :	-292.3186	$kg / rad$

$X_{uq\delta e} :$	-111.7084	$kg / rad^2$
$X_{ur\delta r} :$	-111.7084	$kg / rad^2$
$X_{vv} :$	0.0	$kg / m$
$X_{ww} :$	0.0	$kg / m$
$X_{uv\delta r} :$	9.6267	$kg / (m \cdot rad)$
$X_{uw\delta e} :$	-9.6267	$kg / (m \cdot rad)$
$X_{uu\delta r\delta r} :$	-6.8071	$kg / (m \cdot rad^2)$
$X_{uu\delta s\delta s} :$	-6.8071	$kg / (m \cdot rad^2)$
$X_{uu} :$	-7.2993	$kg / m$
$Y_{pq} :$	24.8072	$kg \cdot (m / rad)$
$Y_{\dot{r}} :$	-24.8072	$kg \cdot (m / rad)$
$Y_{\dot{v}} :$	-292.3186	$kg$
$Y_{ur} :$	319.5267	$kg / rad$
$Y_{wp} :$	292.3186	$kg / rad$
$Y_{uv} :$	-206.2675	$kg / m$
$Y_{uu\delta r\delta r} :$	156.4001	$kg / (m \cdot rad^2)$
$Z_{pr} :$	-24.8072	$kg / rad$
$Z_{\dot{q}} :$	-24.8072	$kg \cdot m / rad$
$Z_{\dot{w}} :$	-292.3186	$kg$
$Z_{uq} :$	-335.0280	$kg / rad$
$Z_{vp} :$	-292.3186	$kg / rad$
$Z_{uw} :$	-206.2675	$kg / m$
$Z_{uu\delta e} :$	-156.4001	$kg / (m \cdot rad)$
$K_{up} :$	-24.3459	$kg \cdot m / rad$
$K_{uu\delta_s} :$	30.7660	$kg / rad$
$M_{rp} :$	215.1516	$(kg \cdot m^2) / rad^2$
$M_{\dot{q}} :$	-215.7824	$(kg \cdot m^2) / rad^2$
$M_{\dot{w}} :$	-24.8072	$kg \cdot m$
$M_{uq} :$	-661.4075	$kg \cdot m / rad$
$M_{vp} :$	24.8072	$kg \cdot m / rad$
$M_{ur\delta_s} :$	0.0	$kg \cdot m / rad^2$

$M_{uv\delta s} :$	0.0	$kg / rad$
$M_{uw} :$	-11.8769	$kg$
$N_{pq} :$	-215.1516	$(kg \cdot m^2) / rad^2$
$N_{\dot{r}} :$	-215.7824	$(kg \cdot m^2) / rad^2$
$N_{\dot{v}} :$	-24.8072	$kg \cdot m$
$N_{ur} :$	-633.7799	$kg \cdot m / rad$
$N_{wp} :$	-24.8072	$kg \cdot m / rad$
$N_{uq\delta s} :$	0.0	$kg \cdot m / rad^2$
$N_{uv} :$	11.8769	$kg$
$N_{uu\delta r} :$	-253.6574	$kg / rad$
$N_{uw\delta s} :$	0.0	$kg / rad$

The values presented in Table B-2 are the coefficients that describe the propulsor simulation model used for this research as a result of a notional propulsor design as in [18].

**Table B-2. Generic Undersea Vehicle Propulsor Simulation Model**

$J_o :$	2.7195	$1 / rev$
$w :$	0.0399	Non-dimensional
$t_{ded} :$	0.3115	Non-dimensional
$T_{ n n} :$	3.3786	$kg \cdot m / rev^2$
$T_{ n V_a} :$	-12.2389	$kg / rev$
$Q_{ n n} :$	0.1130	$kg \cdot m^2 / rev^2$
$Q_{ n V_a} :$	-0.3086	$kg \cdot m / rev$
$D_{prop} :$	0.1910	$m$
$\eta_{stator} :$	0.95	Non-dimensional

## Appendix C

### Baseline Autopilot Controller Gains

The values presented in Table C-1 are those of the baseline autopilot for weight configuration 1A in Table 2-2. These baseline gains remained unchanged as the robustness of the autopilot was assessed for varying weight configurations.

**Table C-1. Baseline Autopilot Controller Gains**

Forward Speed	Yaw Loop Gains		Depth/Pitch Loop Gains			Roll Loop	
$U$ (kt)	$K_{rp}$	$K_{\psi P}$	$K_{qp}$	$K_{\theta P}$	$K_{zp}$	$K_{pp}$	$K_{\phi p}$
10	-0.4247	8.375	-0.8351	10.00	-0.123	0.1775	10.0
11	-0.3861	9.225	-0.7592	11.00	-0.123	0.1576	10.0
12	-0.3539	10.075	-0.696	12.00	-0.123	0.1419	10.0
13	-0.3267	10.925	-0.6424	13.00	-0.123	0.1291	10.0
14	-0.3034	11.775	-0.5965	14.00	-0.123	0.1185	10.0
15	-0.2831	12.575	-0.5568	15.00	-0.123	0.1095	10.0
16	-0.2654	13.425	-0.522	16.00	-0.123	0.1019	10.0
17	-0.2498	14.275	-0.4913	4.90	-0.073	0.0953	10.0
18	-0.2359	9.975	-0.464	4.70	-0.069	0.0895	10.0
19	-0.2235	7.525	-0.4396	4.65	-0.066	0.0844	10.0
20	-0.2123	6.925	-0.4176	4.65	-0.064	0.0798	10.0

## Appendix D

### Mission Command Sequences and Depth Compensation Gains

The mission command sequences presented in Table D-1 are those that were used to assess the robustness of a baseline UV autopilot to changes in the UV's weight configuration. Note that for the purposes of this study, the commanded depth changes were set to three times the overall length of the vehicle or 10.97m.

**Table D-1. Mission Command Sequences**

<b>Steady Level Flight Mission Command Sequence</b>							
Duration (s)	Roll Angle (deg)	Depth (m)	Pitch Angle (deg)	Pitch Rate (deg/s)	Yaw Angle (deg)	Yaw Rate (deg)	Propulsor RPM
20	0	50	45	66	0	66	1140
40	0	50	45	66	0	33	570
<b>Steady Turn Mission Command Sequence</b>							
Duration (s)	Roll Angle (deg)	Depth (m)	Pitch Angle (deg)	Pitch Rate (deg/s)	Yaw Angle (deg)	Yaw Rate (deg)	Propulsor RPM
10	0	50	45	66	0	66	1140
25	0	50	45	66	-90	-66	1140
25	0	50	45	66	0	66	1140
40	0	50	45	33	0	33	570
45	0	50	45	33	90	33	570
45	0	50	45	33	0	-33	570
<b>Steady Depth Change Mission Command Sequence</b>							
Duration (s)	Roll Angle (deg)	Depth (m)	Pitch Angle (deg)	Pitch Rate (deg/s)	Yaw Angle (deg)	Yaw Rate (deg)	Propulsor RPM
20	0	50	45	66	0	66	1140
20	0	60.9728	45	66	0	66	1140
20	0	50	45	66	0	66	1140
45	0	50	45	33	0	33	570
40	0	60.9728	45	33	0	33	570
45	0	50	45	33	0	33	570

The compensation gains applied to the depth commands for the different weight configurations at low and high speed are shown in Table D-2. These compensation gains are multiplied by the desired depth to determine the compensated depth command such that a vehicle perturbed in weight configuration can attain the desired depth without retuning of the autopilot.

**Table D-2. Depth Compensation Gains**

Weight Configuration	Desired Depth: 50 m		Desired Depth: 60.9728 m	
	$U$ : 10kt	$U$ : 20kt	$U$ : 10kt	$U$ : 20kt
1A	1.0000	1.0000	1.0000	1.0000
1B	0.9911	0.9936	0.9926	0.9948
1C	1.0022	1.0016	1.0019	1.0012
2A	0.9907	0.9958	0.9924	0.9965
2B	0.9783	0.9889	0.9822	0.9909
2C	0.9934	0.9974	0.9947	0.9979



## Bibliography

- [1] Fernandes, D. d. A., Soerensen, A., & Donha, D. C. (2014). *Full-Scale Sea Trials of a Motion Control System for ROVs Based on a High-Gain State Observer*. Paper presented at the World Congress.
- [2] Fernandes, D. d. A., Sørensen, A. J., Pettersen, K. Y., & Donha, D. C. (2015). Output feedback motion control system for observation class ROVs based on a high-gain state observer: Theoretical and experimental results. *Control Engineering Practice*, 39, 90-102.
- [3] Shenoi, R. R., Krishnankutty, P., & Selvam, R. P. (2015). *Sensitivity Study of Hydrodynamic Derivative Variations on the Maneuverability Prediction of a Container Ship*. Paper presented at the ASME 2015 34th International Conference on Ocean, Offshore and Arctic Engineering.
- [4] Sen, D. (2000). A study on sensitivity of maneuverability performance on the hydrodynamic coefficients for submerged bodies. *Journal of Ship Research*, 44(3), 186-196.
- [5] Petrich, J. (2009). *Improved guidance, navigation, and control for autonomous underwater vehicles: theory and experiment*. Virginia Polytechnic Institute and State University.
- [6] Fryxell, D., Oliveira, P., Pascoal, A., & Silvestre, C. (1994). *An integrated approach to the design and analysis of navigation, guidance and control systems for AUVs*. Paper presented at the Proc. Symposium on Autonomous Underwater Vehicle Technology.
- [7] Santhakumar, M. (2013). Investigation into the dynamics and control of an underwater vehicle-manipulator system. *Modelling and Simulation in Engineering*, 2013, 17.
- [8] Dannigan, M., & Russell, G. T. (1998). Evaluation and reduction of the dynamic coupling between a manipulator and an underwater vehicle. *Oceanic Engineering, IEEE Journal of*, 23(3), 260-273.
- [9] McEwen, R., & Streitlien, K. (2001). Modeling and control of a variable-length auv. *Proc 12th UUST*.
- [10] Prestero, T. T. J. (2001). *Verification of a six-degree of freedom simulation model for the REMUS autonomous underwater vehicle*. Massachusetts Institute of Technology.
- [11] Evans, J., & Nahon, M. (2004). Dynamics modeling and performance evaluation of an autonomous underwater vehicle. *Ocean Engineering*, 31(14), 1835-1858.
- [12] Feldman, J. (1979). Revised standard submarine equations of motion. David W. Taylor Naval Ship Research and Development Center, Washington DC: DTNSRDC/SPD—O393-09.

- [13] Fossen, T. I. (2002). *Marine control systems: guidance, navigation and control of ships, rigs and underwater vehicles*.
- [14] Goodman, A. (1960). *Experimental techniques and methods of analysis used in submerged body research*. Paper presented at the Proceedings of the Third Symposium on Naval Hydrodynamics.
- [15] Gertler, M., & Hagen, G. R. (1967). *Standard equations of motion for submarine simulation* (No. NSRDC-2510). David W. Taylor Naval Ship Research and Development Center, Bethesda MD.
- [16] Yedavalli, R. K., & SpringerLink (Online service). (2014). *Robust control of uncertain dynamic systems: A linear state space approach* (2014th ed.). New York, NY: Springer New York. doi:10.1007/978-1-4614-9132-3
- [17] Stevens, B. L., & Lewis, F. L. (2002). Aircraft simulation and control. *John Wiley & Sons, New Jersey, USA*.
- [18] Renilson, M. (2015). *Submarine Hydrodynamics*. Springer.

## **Distribution List**

Distribution List for ARL Penn State Technical Report 16-002 titled “A Prescribed Flight Performance Assessment for Undersea Vehicle Autopilot Robustness” by Daniel J. Bowman, dated 16 June 2016

Defense Technical Information Center  
8725 John J. Kingman Rd.  
Suite 0944  
Fort Belvoir, VA, 22060-6218